Available online at www.sciencedirect.com
SCIENCE DIRECT®
Surface Science Reports 60 (2005) 1–53
surface science reports
www.elsevier.com/locate/surfrep

Arsenic-rich GaAs(0 0 1) surface structure

Vincent P. LaBella [a,*], Michael R. Krause [a], Zhao Ding [b], Paul M. Thibado [b]

[a] *College of Nanoscale Science and Engineering, University at Albany-SUNY, Albany, NY 12203, USA*
[b] *Physics Department, University of Arkansas, Fayetteville, AR 72701, USA*

Accepted 6 October 2005

Abstract

This article discusses the past 40 years of research covering the equilibrium thermodynamic properties of the arsenic-rich GaAs(0 0 1) surface, which is the starting surface for producing the majority of optoelectronic devices worldwide. A coherent picture of the observed surface structures, theoretical calculations, and experimental results will be presented. The interplay in surface-free-energy-reduction between reconstruction transformation and roughening is now well understood for the GaAs(0 0 1) surface and will be discussed. The recent confirmations of the structural models for the (2 × 4) and c(4 × 4) reconstructions as well as the discovery of preroughening aid in this understanding.

Keywords: Arsenic-rich GaAs(0 0 1); Scanning tunneling microscopy; Molecular beam epitaxy; Reflection high-energy electron diffraction

Contents

* Corresponding author.
E-mail address: vlabella@uamail.albany.edu (V.P. LaBella).

0167-5729/$ – see front matter © 2005 Elsevier B.V. All rights reserved.
doi:10.1016/j.surfrep.2005.10.001

1. Introduction

This *Surface Science Report* will review the past 40 years of research on understanding the equilibrium thermodynamics of the arsenic-rich GaAs(0 0 1) surface. GaAs(0 0 1) and all compound semiconductor surfaces offer a rich and unique variety of physical phenomena to study which gives fascinating insight into the field of surface science. In addition, the GaAs(0 0 1)-(2 × 4) reconstructed surface is the starting surface for producing the majority of optoelectronic devices worldwide [1]. These devices, or layered heterostructures, are fabricated using epitaxial techniques where layers of atoms are deposited upon an atomically flat and clean substrate under ultra-high vacuum conditions. The growth front of the material and the device is always a surface and the knowledge gained from studying the surface can be utilized to develop predictable models for growth.

Surfaces minimize their free energy through two different methods. Relaxation and/or reconstruction is one method, where the surface atoms move and/or rebond to other surface atoms to form a surface crystal structure with a new periodicity. Reconstruction may also include facet growth on certain clean or adsorbate-covered atomically rough surfaces; surface energy is minimized by the formation of hill-and-valley nanostructures with facets of low-index close-packed orientations. The other method is roughening, where the entropy of the surface is increased by forming nanoscale structures such as islands, or pits. In this method the free energy is lowered due to the increase in entropy, as the temperature is increased.

Determining when a surface will choose one method or another simply from knowing the chemical species, crystal structure, and crystallographic orientation of the surface is nearly impossible due to the complex interdependency of these mechanisms. For example, roughening depends upon nearest neighbor step energies, which can depend upon the reconstruction. It is conceivable that a surface can begin to roughen under one reconstruction as the temperature is increased, but suddenly change reconstructions and become smooth.

The parameter which controls the observed equilibrium state of an ideal surface is the chemical potential of the species which compose the surface; assuming a perfect crystal structure under complete vacuum. For surfaces composed from a single element the substrate temperature controls the chemical

potential (neglecting any adsorbate induced interactions). However, on (0 0 1)-oriented compound semiconductor surfaces such as GaAs(0 0 1) there are two chemicals potentials in need of control: the Ga and the As. Experimentally this is achieved by tuning both the substrate temperature and arsenic flux or beam equivalent pressure (BEP). Modern, commercially available, molecular beam epitaxy (MBE) machines are equipped with substrate heaters and special arsenic ''valved-cracker'' cells that allow the arsenic BEP to be varied over several orders of magnitude (i.e. 0.01–100.0 μTorr) through the use of a needle valve.

This dual chemical potential landscape gives GaAs(0 0 1), and all other (0 0 1)-oriented compound semiconductor surfaces, a broader and potentially richer surface phase space to explore. However, it can also complicate surface preparation which confounds what is ideally sought: determination of the lowest energy structures. To study this complex surface many state of the art experimental and theoretical tools have been brought to bear since the inception of epitaxy on GaAs(0 0 1) in the late 1960s [2–5]. Much insight has been gained with the advent of modern and now commercially available in situ experimental techniques such as the scanning tunneling microscope, electron diffraction, band edge temperature measurements, and molecular beam epitaxy. Because of this vast body of work the interplay between reconstruction and roughening is now well known for the GaAs(0 0 1) surface. However this understanding has only come about very recently due to: (1) the integration these experimental techniques into one complete system, (2) the advent of modern theoretical methods such as density functional theory as well as the increases in computing power needed to carry out such calculations, and (3) our understanding of 2D many body physics and phase transformations.

Due to the enormous body of research that exists on the GaAs(0 0 1) surface, the scope of this review is limited to only those UHV STM and diffraction studies of the equilibrium structures of the arsenic-rich GaAs(0 0 1) surface structures. In addition, theoretical models and methods such as the electron counting model, first principles density functional theory, and 2D many body models will be discussed. This of course excludes a vast body of work on the gallium-rich reconstructions, kinetics, diffusion, etching, adsorbate induced reactions, growth, etc. that is simply too large to fit into one article. The interested reader should refer to other reviews of this and other compound semiconductor surfaces that have been previously published [6–13].

1.1. Surface phase diagram

GaAs is a zinc-blende semiconductor with a direct band gap of 1.42 eV and a lattice constant of 5.65 Å. In the [0 0 1] direction the crystal consists of alternating planes of Ga and As that are separated by 1.41 Å as displayed in Fig. 1. The (0 0 1) surface is a polar surface and can be terminated by either species that form a 4 Å square 1×1 lattice when unreconstructed. A monolayer on the GaAs(0 0 1) surface is a 2.82 Å thick bi-layer composed of both Ga and As.

The arsenic-rich surface reconstructions appear when a clean (0 0 1) surface is heated above room temperature under an arsenic flux or beam equivalent pressure (BEP). The transformations in reconstruction that occur between 400 and 700 °C and arsenic BEPs between 0.1 and 10 μTorr as observed by reflection high-energy electron diffraction (RHEED) and highly accurate (±1 °C) band-edge temperature measurement are plotted in Fig. 2. At low temperatures the surface is in the most arsenic-rich c(4×4) phase and as the temperature is increased under a constant arsenic flux the diffraction pattern changes to a (2×4) then to a (2×1). These transitions are reversible, and also occur when increasing or decreasing the arsenic BEP. The Ga-rich reconstructions (not discussed

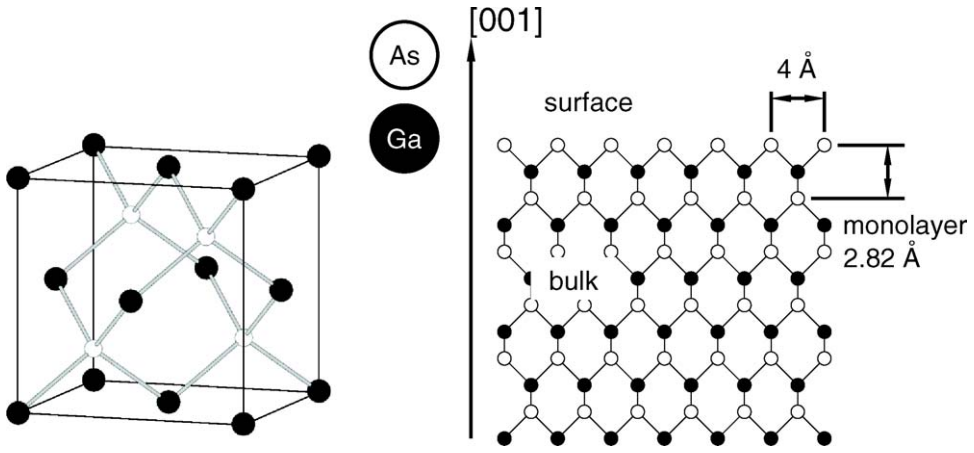

Fig. 1. (Left) GaAs zinc-blende unit cell. (Right) Diagram of the GaAs zinc-blende structure in the ⟨0 0 1⟩ direction. The spacing between layers is 1.41 Å, and the spacing between atoms on the unreconstructed bulk terminated surface is 4 Å.

here) occur under both an arsenic and gallium flux, where the transitions are controlled by the BEP ratio of the two species.

Growth of high-quality crystals for optoelectronic devices occurs in the 2×4 phase around 580–600 °C. Low temperature grown (LTG) GaAs is grown on the c(4×4) reconstruction between 200 and 300 °C which is used in a variety of exotic applications such as transition metal doped GaAs for ''spintronic'' applications, or extremely high resistivity and very short carrier lifetime applications [14–17]. The changes in reconstruction occur because the chemical potential of the two species are changing

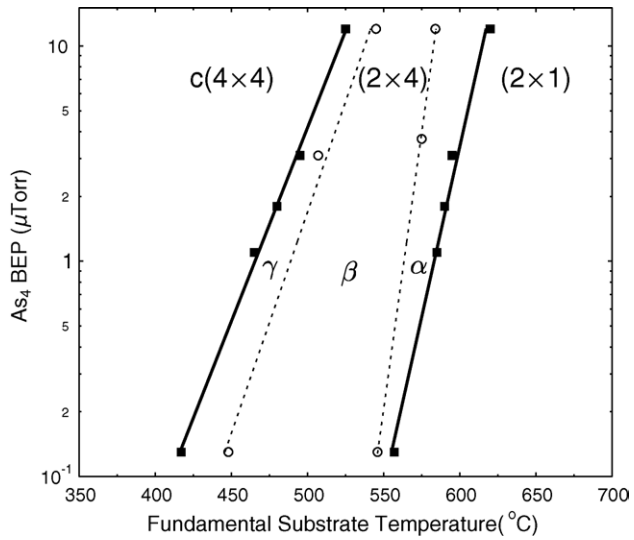

Fig. 2. Surface reconstruction phase diagram of the arsenic-rich GaAs(0 0 1) surface as measured using reflected high-energy electron diffraction and the band-edge temperature measurement technique. The solid lines indicate the transitions between the three reconstructions as indicated. The dotted lines indicate the transitions between the three sub-phases of the (2×4) reconstruction. Reprinted with permission from [18]. Copyright 2001, AVS The Science and Technology Society.

due to the changes in substrate temperature and arsenic BEP. This map of reconstructions versus substrate temperature and arsenic BEP is typically called a surface phase diagram.

Understanding the equilibrium structure of these three reconstructions will be the focus of this article. To prepare these surfaces for imaging with STM at room temperature the surface is annealed at the desired point in the phase diagram for a desired amount of time and then quenched to room temperature at a rate of 1–2 °C/s. During this quenching process it is important to decrease the arsenic BEP by closing the valve to keep the chemical potential ratio of the two species relatively constant. This procedure has been shown to be successful at freezing in the high temperature surface morphology.

1.2. Rules for semiconductor surface reconstructions

During the discovery of the reconstruction phases of the GaAs(0 0 1) surface, the theoretical rules for semiconductor surface reconstructions were also forming [19,20]. These rules are broadly applicable to all semiconductor surfaces and can give insight into whether a given surface reconstruction can appear on a given semiconductor surface. The specific rules for compound semiconductor surfaces are as follows:

i. The surface structure observed will be the lowest free-energy structure kinetically accessible under the preparation conditions.
ii. Surfaces tend to be autocompensated.
iii. For a given surface stoichiometry, the surface atomic geometry is determined primarily by rehybridization induced lowering of the surface state bands associated with either surface bonds or (filled) anion dangling bonds.

Rule ii is often called the electron counting model (ECM). It means that a polar compound semiconductor surface such as the GaAs(0 0 1) surface will only form structures whose dangling-bond valence band states are filled and dangling-bond conduction band states are empty. In other words, the surface must remain non-metallic with a band gap at the surface, neglecting the effects of defects. It should be noted that this model works well for GaAs(0 0 1) and InP(0 0 1) however antimony and nitrogen based compound semiconductors have been shown to violate this rule [21–24].

To see how the ECM is used to determine the allowed surface reconstruction, the electrons in the surface unit cell must be counted for a given reconstruction. If this reconstruction is allowed, the number of electrons needed to fill all the bonds must be equal to the total number of electrons that are available from the atoms that compose the reconstruction. Consider a surface composed of dimers of anions formed in rows similar to the (2×4) reconstruction (cf. Fig 15). Each dimer requires the following number of electrons: 2 in the dimer bond, 2 in each of the two dangling bonds, and 8 to bind the dimer to the atoms underneath, for a total of 14. Each dimer has the following number of electrons available to it: $2V_n$, where V_n is the number of valence electrons in the anion, and $2V_p/2$, where V_p is the number of valence electrons in the cation. Even though each dimer is bound to 4 underlying cations it shares these cations with the neighboring dimer and the underlying cations contribute only half their total number of electrons since the other half are used to bind them to the third layer. Therefore the total number of electrons available per dimer is $2V_n + V_p$.

A unit cell composed of N dimers that span A surface lattice constants in the direction perpendicular to the dimer bond or a $(2 \times A)$-reconstruction, results in the following electron balance equation:

$$14N = (2V_n + V_p)N + (A - N)V_p, \tag{1}$$

where the last term $(A - N)V_p$ accounts for the extra cation electrons from the missing dimers. For III–V surfaces with $V_p = 3$ and $V_n = 5$ this equation reduces to

$$4N = 3A. \tag{2}$$

The (2×4) unit cell ($N = 3, A = 4$) with three dimers is the smallest unit cell to satisfy this requirement. This indicates that a surface composed of only one dimer ($N = 1, A = 1$) such as a (2×1) is forbidden, making it unlikely that a periodic surface reconstruction is the cause of the (2×1) RHEED pattern observed in Fig. 2. A c(4×4) with three As dimers on top of a full plane of arsenic also satisfies the ECM since the three dimers generate three extra electrons which satisfy the needs of the four As dangling bonds due to one dimer vacancy (cf. Fig. 12) [25].

2. Experimental methods

The understanding of the GaAs(0 0 1) surface followed directly from improvements in scientific instrumentation. This section gives a brief overview of the current state of the art in the pertinent experimental techniques and equipment used to prepare and study GaAs(0 0 1) surface.

2.1. Molecular beam epitaxy (MBE)

Molecular beam epitaxy (MBE), a refined form of vacuum evaporation, was developed in the late 1960s as a means of growing high-purity epitaxial layers of compound semiconductors [2–5]. Since that time it has evolved into a popular technique for growing III–V compound semiconductors as well as several other materials. As a crystal growth technique performed within an UHV environment ($<1 \times 10^{-9}$ Torr), MBE can produce high-quality single crystal layers with very abrupt interfaces and excellent control of thickness, doping, and composition. Because of this high degree of control, it is a valuable tool in the development of layered heterostructures used to manufacture sophisticated electronic and optoelectronic devices.

In MBE, the neutral atomic and molecular beams of source material impinge on a heated substrate under UHV conditions. The substrate is mounted on a rotatable manipulator that contains a heater and a thermocouple located between the substrate and the heater to measure the substrate temperature. High purity source materials are individually placed in separate crucibles made of an inert material such as pyrolytic boron nitride (PBN). The crucibles are housed in Knudsen cells and are heated to a temperature where the vapor pressure of the material is significant enough to create the desired flux of molecules. Since the chamber is under UHV, the molecules travel in a straight line before striking the substrate. Growth will continue until the path of the molecules is blocked, which is accomplished using mechanical shutters placed in front of the cell opening. The shutters are fast-acting and can open or close in about 0.5 s. The growth rate of the material can range from monolayers per second to monolayers per minute allowing for atomic layer control of the thickness of the desired epilayer.

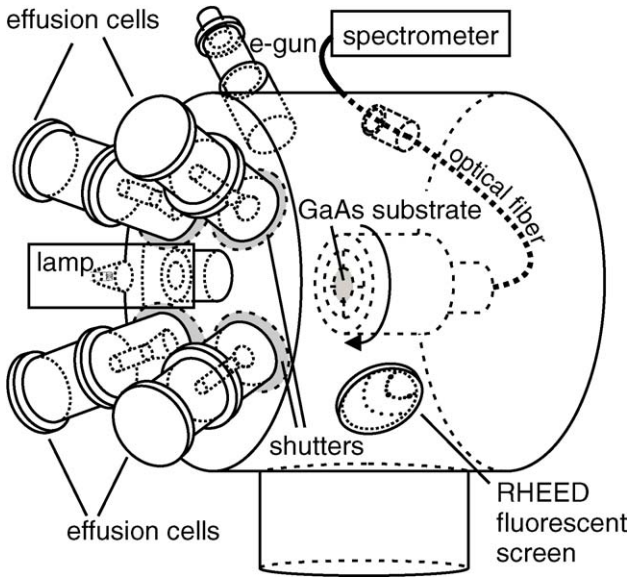

Fig. 3. Diagram of a typical MBE system growth chamber containing effusion cells for the source materials, shutters, and substrate holder. The electron gun and screen are for surface monitoring using RHEED. The lamp, optical fiber, and spectrometer are for band edge temperature measurements. Reprinted with permission from [26]. Copyright 2005, AVS The Science and Technology Society.

The group III elements (Ga, In, Al) and dopant materials (Si, Be) are typically housed in Knudsen cells where the flux emanates from an open orifice that is blocked by a mechanical shutter. In contrast, the group V elements (As, P, Sb) are housed in special ''valved cracker'' cells that keep the material in a continuously evaporative state and control the flux to the substrate with a UHV-compatible needle valve. This allows for both complete elimination of the group V flux and precise control of the BEP over a very broad dynamic range (i.e. 0.01–100.0 μTorr), which is required to grow high-quality crystals. Past the valve, a hot filament, or cracker, can be used to break apart the molecules in the beam into lower mass species (i.e. As_4 to As_2). The BEP is measured using an ion gauge which can be rotated into and out of the molecular beams. A drawing of a typical MBE chamber with the substrate heater, cells, and shutters is displayed in Fig. 3. This drawing also displays reflection high-energy electron diffraction (RHEED) equipment used to monitor surface quality and growth rate and a spectrometer for highly accurate band edge temperature measurements. These two techniques will be discussed in the following sections.

2.1.1. Growth rate

During MBE growth of GaAs the arsenic flux is oversupplied, typically 10–100 times larger BEP than the Ga. The sticking coefficient of arsenic on an arsenic terminated GaAs(0 0 1) surface is zero thereby inhibiting the growth of bulk arsenic. Therefore, the arrival rate of Ga atoms controls the growth of GaAs, which can be controlled by the cell temperature and stopped abruptly with the shutter. The growth rate of the source material is dominated by the material's vapor pressure which is controlled by the cell temperature. The vapor pressure is a measure of the number of atoms leaving the surface of the material as a function of temperature. The complete temperature dependence of vapor pressure is given by an

empirical formula with four adjustable constants:

$$\log(P) = A - \frac{B}{T} + CT + D\log(T), \tag{3}$$

where T is the absolute temperature and A, B, C, and D are the four fitting parameters. These fitting parameters have some physical significance, for instance, the constant B is closely related to the energy required to remove an atom from the surface, i.e., the activation energy, and D is related to the molar heat capacity for the material. Values of the parameters are given in Ref. [27].

Geometrical factors also need to be considered such as the distance from source material to the substrate, which is typically on the order of half a meter. This is the dominant geometrical factor and changes over time as material is evaporated or inadvertently shifts in the crucible. To develop an equation that relates the material temperature to the desired growth rate which accounts for the material's vapor pressure as well as the geometrical factors the dominating terms from Eq. (3) are kept and a geometrical factor is introduced yielding:

$$G(T) = G_0 \times 10^{E_a/k_B T} T^B, \tag{4}$$

where G is the growth rate, G_0 the geometrical term, E_a the energy required to remove one atom from the surface of the charge, and B is a fitting parameter. The growth rate of GaAs as measured using RHEED oscillations at four Ga cell temperatures is plotted with a fit to Eq. (4) and shown in Fig. 4.

2.2. Band edge temperature measurement

Substrate temperature is a critical parameter for MBE growth and surface preparation. It is also the most difficult to measure and control, because the thermocouple that is typically used cannot be in good thermal contact with the substrate if one wants to produce high-quality, high-uniformity material. The inaccuracies in substrate temperature affect the ability to transfer growth recipes from one chamber to

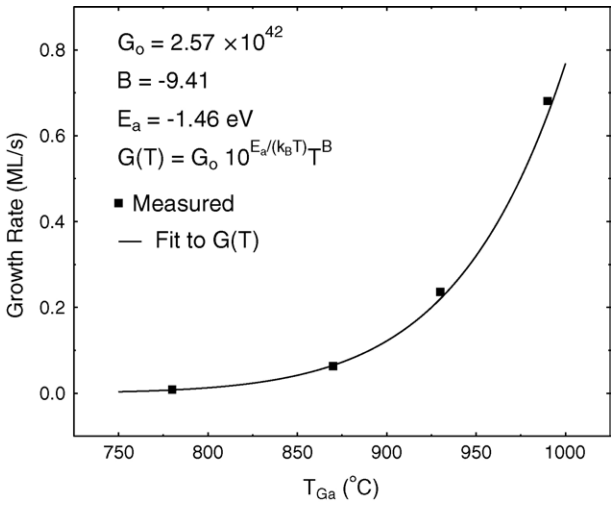

Fig. 4. The growth rate of GaAs as a function of Ga cell temperature as measured using RHEED oscillations at four Ga cell temperatures and corresponding fit to the indicated function.

another which hinders the progress in MBE. Optical pyrometry is often used for substrate temperature determination and is more accurate than a thermocouple. However, the accuracy of pyrometers is limited by stray light from the source ovens and substrate heater filaments. In addition, pyrometer readings are affected by films deposited on the pyrometer viewport and by lack of knowledge of sample emissivity, which in many cases is changing during the growth of the structure. Finally, the direct radiative heating of the substrate floods the pyrometer with the infrared radiation of the heater filaments, making the technique even less accurate [28].

Other workers have suggested the use of fundamental optical properties, such as the band gap of a semiconductor and its temperature dependence, as a vehicle for obtaining accurate and reproducible substrate temperatures [28]. The most successful non-contact temperature measurement scheme was achieved by installing an optical fiber inside the MBE system that allows an alternate light source to be brought to the back or front side of the substrate which is now a standard option on commercially available MBE machines [29,30]. The transmitted light is then collected and fed to a spectrometer using an optical fiber as shown in Fig. 3. Utilizing a separate white light source other than the light from the heater filament allows the background infrared blackbody radiation from the heater filaments, which can wash-out the substrate band edge, to be removed by chopping the light. In this way, the fundamental band gap of the substrate can be measured very accurately from the transmission spectra. The transmission spectra are recorded in real time by a spectrometer and fed to a computer to measure the substrate temperature by comparing the spectra to a pre-determined temperature calibration database. This approach allows the substrate temperature to be measured very accurately $\pm 1\,^{\circ}\mathrm{C}$ over a wide-temperature range (100–700 °C for GaAs) without making physical contact with the substrate. The rate at which temperature measurements can occur is about $10\ \mathrm{s}^{-1}$ which is more than adequate for growing crystals. A software proportional-integral-derivative (PID) feedback loop can be used to control the power supplied to the substrate heater based upon the desired temperature of the substrate as measured by the band-edge thermometer.

To demonstrate the sensitivity of the band-edge measurement technique the power to the substrate heater was maintained at a constant value which gave a constant sample temperature of 580 °C. Then the shutter to the Si effusion cell, held at a temperature of 1300 °C, was opened for 3 min then closed. During this time the substrate temperature was measured by both the band edge system and thermocouple. Surprisingly, the substrate temperature as measured with the band edge technique experiences a $\sim 12\,^{\circ}\mathrm{C}$ increase as displayed in Fig. 5, whereas the thermocouple temperature remained constant. The substrate returned to 580 °C when the Si shutter was closed. The increase in temperature is due to the sample absorbing the radiative heat from the Si effusion cell which may be adversely effecting the deposition quality during the growth process.

The key advantage of incorporating an optical transmission temperature measurement system into a MBE chamber is fast and accurate temperature determinations, which are derived from a fundamental optical property. Thus, temperature measurement is not subject to variations due to different substrate mounting strategies or even which MBE machine is used to perform the measurement.

2.3. Reflection high-energy electron diffraction (RHEED)

Reflection high-energy electron diffraction (RHEED) is utilized for in situ real-time determination of the surface structure, surface quality, and growth rate of the material during MBE growth. In RHEED, an

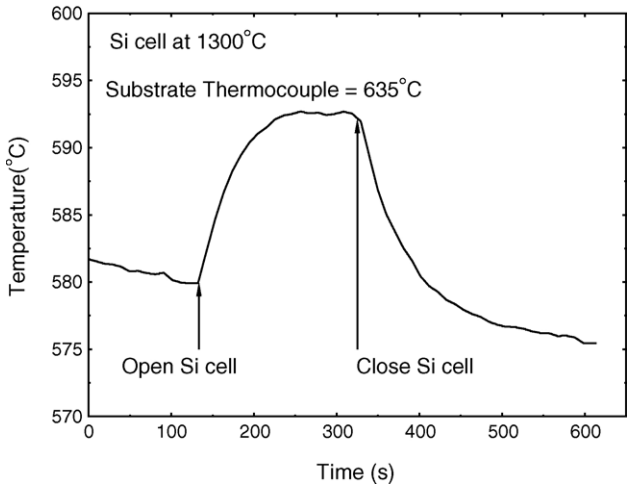

Fig. 5. Band-edge thermometry temperature plotted vs. time while the shutter to the Si effusion cell was opened and then closed. A constant-current power supply maintained the substrate heater filament at a constant temperature of 580 °C. The increase in sample temperature is due the radiation emitted from the Si cell which is at 1300 °C. Interestingly, the thermocouple temperature remained constant at 635 °C while the Si shutter was open. From LaBella et al. [31].

electron beam with an energy ~ 10 keV strikes a single crystal surface at a glancing angle (~ 1–$3\,^\circ$). The reflected beam forms a diffraction pattern on a screen (cf. Fig. 3). This geometry is compatible with MBE growth since the front of the sample is open for the flux of material from the effusion cells permitting use during deposition. The electrons only penetrate the first few monolayers of the material due to the glancing incidence which makes RHEED highly surface sensitive. The diffraction intensity is instantly displayed on a screen allowing for in situ real-time analysis.

To identify the various reconstructions of the GaAs(0 0 1) surface as displayed in Fig. 2, RHEED patterns must be acquired in three azimuths 45° apart ([$\bar{1}$ 1 0], [0 1 0], and [1 1 0]), due to the cubic symmetry of GaAs and the directional nature of RHEED. The patterns are then classified by the number of spots that appear in addition to the primary spot. A pattern that only shows the primary spot is called a $1\times$ "one-by", and patterns with n additional spots in between the primary spots are called $(n+1)\times$. The additional spots indicate a structural spacing of $(n+1)\times$ greater than the unreconstructed surface lattice spacing due to the reconstruction. The reconstructions are classified by these three patterns. A table of four GaAs(0 0 1) reconstructions and their corresponding directional RHEED periodicities along with examples of a $1\times, 2\times$, and $4\times$ RHEED patterns are displayed in Fig. 6. An Ewald sphere construction can also be utilized to understand the resulting diffraction patterns and has been documented elsewhere [9].

The appearance of the RHEED diffraction pattern provides qualitative feedback on surface morphology. If the surface is atomically flat, then the RHEED diffraction patterns appear "spotty", similar to what is seen in Fig. 6. If the surface is rough, then the horizontal streaks are more "streaky". The reason for this is that the steps limit the long-range order on the surface, which broadens the reciprocal lattice rods in a direction parallel to the surface. Due to the low incident angle of the electrons ($\sim 3\,^\circ$), the reciprocal lattice rods are nearly tangent to the Ewald spheres. If the reciprocal lattice rods are infinitely narrow (corresponding to an atomically flat surface), the intersections of the rods with the Ewald sphere

	[110]	[010]	[$\bar{1}$10]
c(4×4)	2×	4×	2×
2×4	2×	1×	4×
c(2×8)	2×	2×	4×
2×1	2×	1×	1×

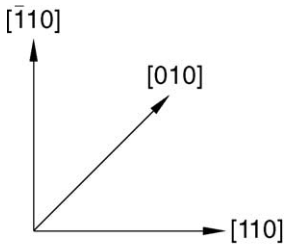

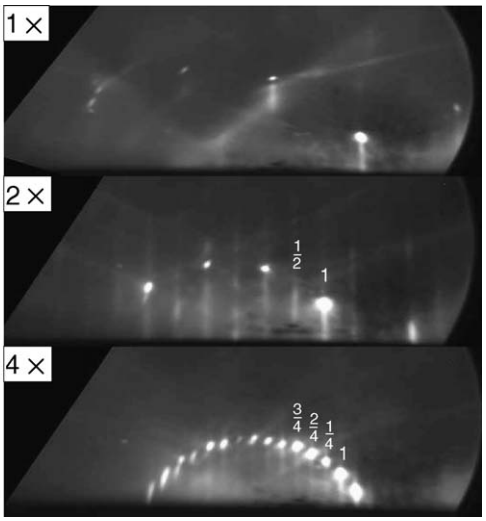

Fig. 6. (Left) Table of four surface reconstructions and their corresponding RHEED periodicities. (Right) Example of 1×, 2×, and 4 ×GaAs(0 0 1) RHEED patterns with the order of the spots as indicated.

will still be approximately points, and the RHEED image will appear ''spotty''. If the rods have some width, however, the intersections broaden out into ''streaky'' pattern. An amorphous surface, such as an oxide layer, shows a haze instead of a diffraction pattern and polycrystalline surfaces result in rings circling the straight-through beam. Such information, although only qualitative, can be a useful check of the surface condition.

2.3.1. Growth rate determination

RHEED intensity oscillations can be used as an accurate, quick, direct measure of the growth rates in MBE. When growth is initiated on a smooth GaAs surface, the intensity of the RHEED pattern, especially the specular reflection, starts to oscillate. The oscillation frequency corresponds to the monolayer growth rate [32]. The oscillations can be explained by a layer-by-layer growth mode as demonstrated in Fig. 7. When a layer starts the surface is smooth and the specular spot is bright, but as the next layer nucleates, islands form on the surface decreasing the specular spot intensity. As the layer finishes, the islands coalesce into a flat layer, and the specular spot intensity increases. The oscillation of the specular spot intensity has been attributed to the oscillating roughness of the layers changing the diffuse scattering, but the incident angle dependence of the oscillations suggests that interference between electrons scattering from the underlying layer and the partially grown layer contribute to these oscillations [33].

2.4. Scanning tunneling microscopy (STM)

Scanning tunneling microscopy (STM) was invented in the early 1980s by Binnig and Rohrer at IBM in Zurich [34,35]. STM provides a picture of the atomic arrangement of a surface by sensing changes in the topography and changes in the local electron density of surface states. It has the unique ability to determine structural and electronic information of the surface on an atomic scale. STM images not only display the geometric structure of the surface, but also depend on the electronic density of states of the

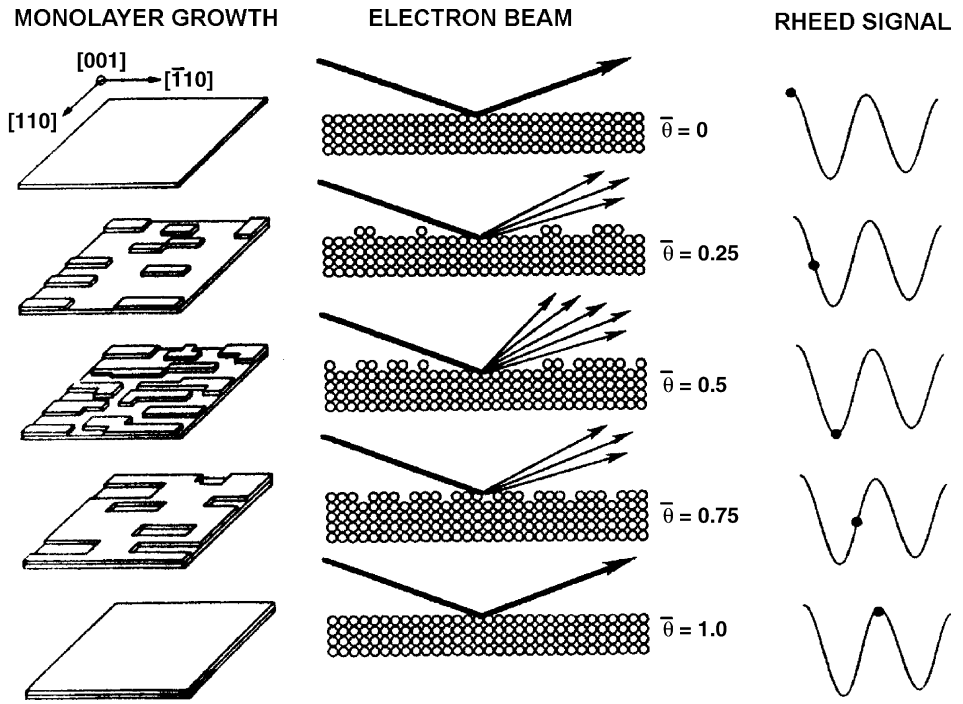

Fig. 7. Illustration of the mechanism for RHEED specular spot oscillations during growth of a monolayer. Reprinted from [33], Copyright (1992), with permission from Elsevier.

sample, as well as on the complex tip–sample interaction mechanisms. In this way, STM provides a ''real-space'' view of a surface complimentary to diffraction methods.

In STM an atomically sharp tip is brought within a few Angstroms of a conducting surface using piezoelectric actuators, which creates an energy barrier for electrons between the tip and the sample as displayed in Fig 8(a). A potential difference U of a few volts is applied between the tip and sample which lowers the energy barrier increasing the probability that the electrons can quantum mechanically tunnel through the barrier. The net flow of tunneling electrons can be measured as a current, which is proportional to the transmission probability. Within a simple model, the expression for tunneling current

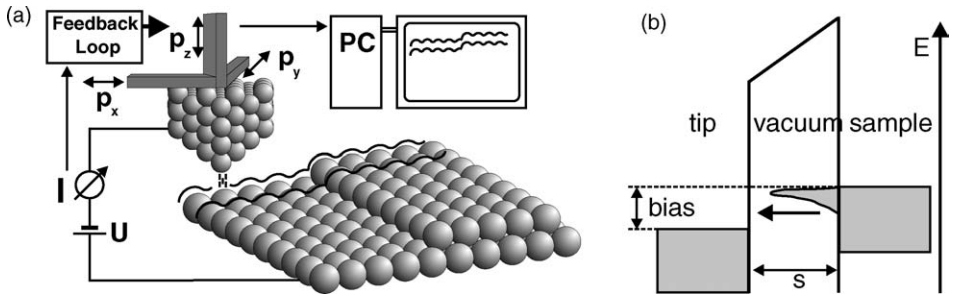

Fig. 8. Schematic representations of (a) the major components an STM: conducting sample, STM tip, piezoelectric actuators. (b) The energy band in the semiconductor and the tip for filled state tunneling which is utilized to image the GaAs(0 0 1) surface.

can be shown to be

$$I \propto e^{-2s\sqrt{2m\phi}/\hbar}, \tag{5}$$

where m is the mass of the electron, $\hbar$ is the Planck's constant, ϕ is the effective barrier height, and s is the tip-to-sample separation distance.

Imaging is accomplished by measuring the tip height as the tip is raster scanned across the surface. A feedback circuit is utilized, which adjusts the tip height using piezoelectric actuators such that a constant current is maintained. As a result of the exponential sensitivity of the tunneling current, a highly detailed image of the surface topography is generated. Since the tip probe is sensitive to locations into (or out of) which electrons can tunnel, STM images are pictures of the local density of states (LDOS) at the surface. These states may, or may not correspond to actual atomic positions. Special care must be taken to isolate the STM from environmental influences such as floor vibrations. In addition, operation under UHV eliminates surface contaminates which interfere with the stability of the tunneling process.

The net tunneling current depends upon the total number of sample and tip surface electronic states that overlap within the energy range of the tunneling electrons. When a positive bias voltage is applied to the sample (or conversely, a negative voltage is applied to the tip), electrons in the occupied states within the tip can tunnel into the empty states within the conduction band of the sample. Similarly, a negative sample bias allows electrons within the filled states of the sample to tunnel into empty states within the tip. When tunneling occurs from sample to tip as schematically displayed in Fig. 8, the result is a filled-state topographic image. Tunneling from tip-to-sample provides an empty-state image.

The ultimate lateral resolution of STM is on the order of 1 Å and is governed by the sharpness of the tip and quality of the surface. The vertical resolution is governed by the exponential dependence of the tunneling current upon the gap distance and the resolution of the piezo/feedback loop, and is on the order of 0.1 Å. For imaging GaAs(0 0 1), imaging the filled states with tips manufactured from single-crystal ⟨1 1 1⟩-oriented tungsten wire gives the best resolution. The wire is electrochemically etched under high magnification ($\sim 1000\times$) to a sharp point and then electron-beam heated in situ to remove any oxide.

2.5. Integrating MBE and STM

Combining MBE with in situ STM has been accomplished in several systems [36–39,26]. The common approach is to custom build the MBE [38] and/or the STM [36,37], which limits the development of these systems to experts in the relating domain. A different approach is to connect two commercially available MBE and STM facilities via a third custom built UHV chamber [39,26]. In this method only the sample holders and transfer mechanisms must be customized, which is more straightforward than building an entire MBE or STM system. A scaled drawing of such an interconnected system is displayed in Fig. 9. The modifications can be implemented such that in their respective chambers the MBE and STM sample holders can still function in the conventional way. One benefit of this approach is that it allows for the independent operation of the MBE and STM, while avoiding contamination and vibration problems, as well as electrical and thermal noise problems inherent to placing an STM inside a growth chamber.

The current MBE standard for sample mounting and manipulation is a circular 3 in. diameter molybdenum wafer holder which will be referred to as a 'Mo-block' throughout this section. Standard STM sample plates are usually much smaller, for example, a tantalum plate of 18 mm × 15 mm [39,26].

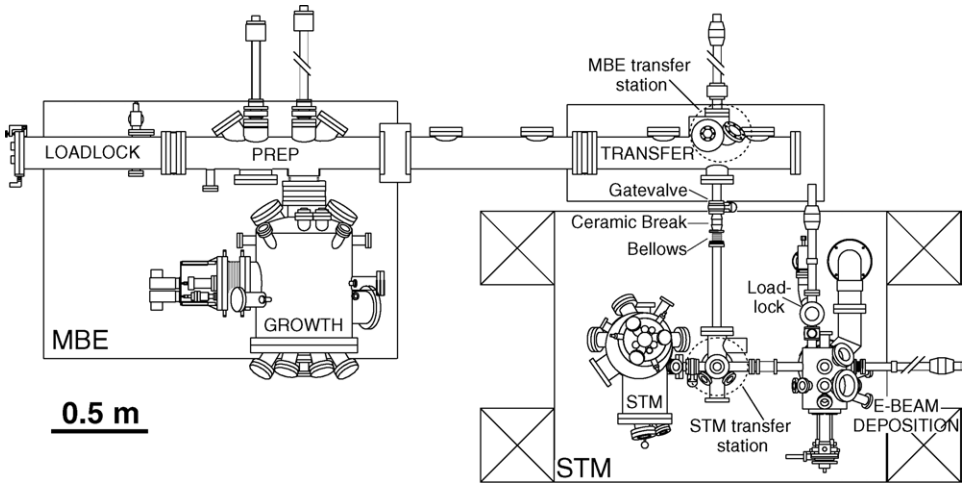

Fig. 9. Scaled drawing of the MBE–STM UHV system. The MBE and the STM facility are separated by about 1 m and are operating completely independent from each other. The customized transfer chamber enables exchange of samples between the MBE and the STM while maintaining UHV conditions. The entire STM chamber rests on an active vibration isolation table. The legs of this table are indicated by the four squares with a cross. Reprinted with permission from [26]. Copyright 2005, AVS The Science and Technology Society.

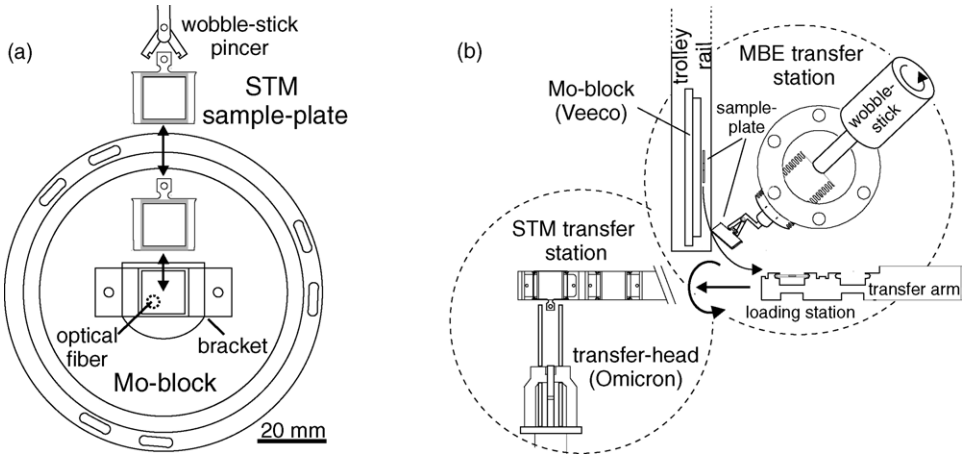

Fig. 10. (a) Scaled drawing of the customized STM plate and Mo-block as indicated. In the STM system the sample plate is held by an eyehole on the top of the plate. In the MBE transfer station a customized wobble stick mounts the STM sample plate onto a bracket on the MBE Mo-block. The Mo-block itself is mounted and transferred using the six slots located towards its outer edge. The dotted circle indicates the position of the optical fiber when the block is mounted in the MBE growth chamber. (b) Sketch of the transfer between MBE and STM chamber. In the MBE transfer station a custom designed wobble stick grabs the STM sample plate from the Mo-block mounting bracket. After being rotated by 90° the STM sample plate can be mounted into the loading station. A magnetic transfer arm translates the loading station all the way to the STM transfer station and rotates it by 90° to allow for the transfer head to pull the sample plate out of the loading station (figure not to scale). Reprinted with permission from [26]. Copyright 2005, AVS The Science and Technology Society.

The MBE Mo-block is transferred and mounted using radially oriented pins, while the STM sample plate is held by an eye hole situated on the top side of the mount [see Fig. 10(a)]. To enable MBE growth on a wafer mounted on an STM sample plate, a custom designed mounting bracket has been attached to the Mo-block to insert the STM sample plate as shown in Fig. 10(a). In the center of the Mo-block and the STM sample plate, square holes have been machined out to allow for the sample to be radiatively heated from the backside and allow for the band-edge temperature measurements as discussed previously.

Within the MBE chamber and on the trolley rail, which extends from the MBE loadlock to the MBE transfer station [see Fig. 9], the STM sample plate is mounted onto the bracket of the Mo-block. In the MBE transfer station it can be taken off the Mo-block to be transferred into the STM chamber. A special wobble stick has been designed to grab the STM sample plate with off center double jaw pincers, which are fully rotatable, and lift it out of the mounting bracket of the Mo-block. It then rotates the plate by 90° to mount it onto the loading station [see Fig. 10(b)]. The loading station has two mounting brackets to transfer two sample plates at a time. This enables exchanging of sample plates (old sample out–new sample in) with a single transfer process. A transfer arm slides the loading station through a gate valve, edge-welded bellows and a ceramic break into the STM transfer station. After rotating the loading station by 90° in the STM transfer station it can be accessed by the standard STM transfer head, which grabs the sample plate to transfer it via another wobble stick into the STM sample stage.

The gate valve simply allows for the transfer chamber and the STM chamber to be separately vented. The bellows reduce vibrational coupling between the two chambers and the ceramic break isolates them electrically. In addition, the bellows assure that the connection between the STM chamber and the transfer chamber is not rigid. This is necessary since the STM chamber rests on an active vibration isolation table which moves up/down slightly when the vibration isolation is switched on/off, whereas the transfer chamber rests on the floor [26]. The design of the interconnection chamber and the modifications of the original sample holders enable both facilities to be utilized with all their functionalities. The additional integration of an active vibration isolation table demonstrates that the MBE and STM facilities can be combined in environments with considerable building and/or floor vibration.

3. Arsenic-rich reconstructions

The arsenic-rich GaAs(0 0 1) surface reconstructions consist of the c(4 × 4) and the $2 \times 4/c(2 \times 8)$. This section will separately review the experimental and theoretical research that has occurred for each reconstruction to determine the structure of the surface unit cell.

3.1. c(4 × 4)

The GaAs(0 0 1)-c(4 × 4) surface is usually produced by cooling down a (2 × 4) reconstructed surface in an arsenic flux, but can also be observed under rather extreme growth conditions of high As/Ga flux and low substrate temperatures. This is the growth parameter regime of the so-called low temperature grown (LTG) GaAs, which has the potential for designing devices with special properties like extremely high resistivity, very short carrier lifetimes and a large electro-optic effect [14,15]. Recently LTG GaAs has gained additional interest due to the possibility to include high concentrations of magnetic impurities in the lattice, and the discovery of carrier-mediated ferromagnetism in these materials, which can be grown by using the GaAs(0 0 1)-c(4 × 4) surface as a starting point [16,17].

The first observation of the GaAs(0 0 1)-c(4 × 4) reconstruction dates back to the early experimental studies of GaAs homoepitaxy. First a structure with (4 × 4) symmetry was reported for very large As_2/Ga ratios [40–42]. Later on the c(4 × 4) reconstruction was primarily identified using LEED, AES, and RHEED [43,44]. The chemical composition and structure of the c(4 × 4) phase have been further studied with photoemission spectroscopy [45–48], RHEED [47,49–52], and LEED [53,54]. A summary of references using these and other techniques to study the main surface reconstructions on the GaAs(0 0 1) surface has been given in Table 2 of Ref. [12].

The first theoretical investigation that was devoted to the structural identification of the c(4 × 4) reconstruction more than two decades ago suggested that the surface consisted of equal numbers of symmetric and asymmetric As dimers on top of a bulk-like Ga terminated surface [55]. However, this initial structural model of the c(4 × 4) reconstruction by Chadi et al. failed to explain, that the c(4 × 4) exists in a wide range of As coverage as first suggested by Massies et al. [53], and was soon questioned by Larson et al. who performed a combined RHEED and photoemission study [47]. They found that the c(4 × 4) structure has a surface As population greater than 1 ML and can be maintained over a rather wide range of excess As coverage [47]. The excess As is bonded to As only, not to Ga. From their findings they derived a model including two different coexisting c(4 × 4) unit cells with one and two additional As dimers trigonally bonded on top of an As terminated surface (see Fig. 11(a) and (b)). Variable combinations of those two unit cells explain the existing wide range of As coverages observed for the c(4 × 4) structure.

This model was modified by Sauvage-Simkin et al. who performed a grazing incidence X-ray diffraction study of the GaAs(0 0 1)-c(4 × 4) surface [56]. They were the first to establish a six atom

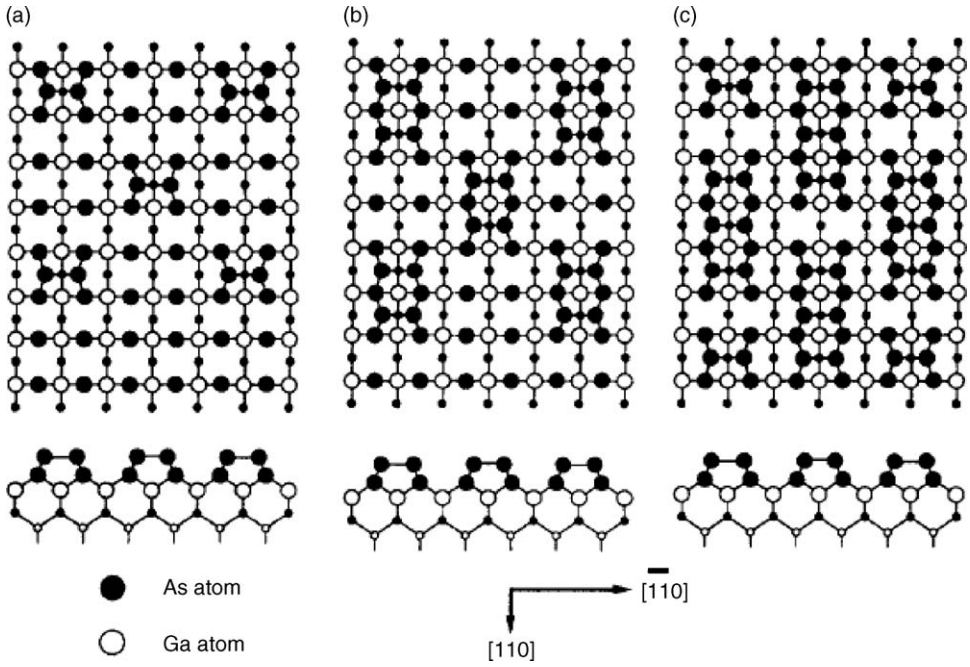

Fig. 11. Ball-to-stick models proposed for the GaAs(0 0 1)-c(4 × 4) surface. Reprinted from [13], Copyright (1997), with permission from Elsevier.

cluster model of three As dimers per c(4 × 4) unit cell oriented along the [1 1 0] direction. The three As dimers are residing on top of a complete As layer, resulting in an additional As coverage of 0.75 ML (see Fig. 11(c)). Again, a combination of unit cells with two and three (instead of one and two) As dimers chemisorbed on top of an As terminated surface is introduced to explain how the c(4 × 4) structure can occur over a large range of As coverages (Fig. 11(b) and (c)). Kamiya et al. suggest that the two-dimer model may be just a transitional stage towards more Ga rich structures [57]. A combined temperature programmed desorption (TPD) and RHEED study achieved a very accurate determination of the coverage range of the c(4 × 4) surface of 1.28–1.61 ML suggesting that a mixture of the one-dimer and the three-dimer structure is present on the surface [58]. Using shadow-cone-enhanced secondary-ion mass spectrometry (SIMS) Xu et al. conclude that the three As-dimer model contains both tilted and untilted dimers [59].

In the first STM study of in situ grown GaAs(0 0 1) surfaces Biegelsen et al. find only evidence of the structure with three As dimers per c(4 × 4) unit cell (six atom cluster Fig. 11(c)) [60]. According to this study, the large range in composition of the c(4 × 4) phase could be caused by two possible factors: (1) a mixture of c(4 × 4) and (2 × 2) units that they have directly observed, which is in agreement with the observation of a c(4 × 4) RHEED pattern since the diffraction spots of the (2 × 2) are a subset of the c(4 × 4), or (2) by an underlying layer containing Ga atoms as well as As.

Further STM studies carried out by different groups could reproduce the basic features of the three-dimer model [61–64]. Avery et al. carried out a detailed investigation of the transition from a (2 × 4) to c(4 × 4) surface with increasing amounts of As. It was determined that depending on the preparation conditions 8–30% of the As atoms in the topmost layer are missing from the basic six atom unit of the three neighboring dimers [63]. But mostly single As atoms are missing rather than dimers indicating that the one-dimer and two-dimer models proposed earlier [47,56] are not stable. Avery et al. also proposed a new structural model with a mixed third layer (25% As and 75% Ga) while the outer two layers contain As only. Utilizing UHV STM and/or other methods several other studies of the phase transition between the (2 × 4) and the c(4 × 4) reconstructions followed with different results. Some confirmed the structural model of the c(4 × 4) reconstruction proposed by Biegelsen et al. [65–67]. Other groups argue that the c(4 × 4) surface does not result from a simple adsorption of As dimers on the (2 × 4) units, but rather forms after the (2 × 4) unit cells are *melted* [68–70]. Bell et al. showed that species intermixing in the second layer of the c(4 × 4) reconstruction is inevitable, with around 25% of the As atoms replaced by Ga [69]. In addition, it was determined that the (2 × 4) to c(4 × 4) transition leads to a roughening of the surface since the c(4 × 4) structure is an intrinsically multilayered reconstruction.

A high-resolution medium-energy ion scattering (MEIS) study provided evidence that the observed c(4 × 4) reconstruction is more Ga rich than predicted by the three-dimer model [71,72]. Falta et al. concluded that the standard three-dimer model must be modified by replacing several As atoms by Ga in the second layer and possibly also in the first layer to achieve agreement with their data. This conclusion drew some controversy in that it did not agree with published STM images [73,74]. Photoemission studies of the GaAs(0 0 1) c(4 × 4) reconstruction also find a surface signal attributed to Ga atoms on the surface supporting a mixture of Ga and As in the topmost layer [75,76]. Work function measurements have been performed for several of the GaAs(0 0 1) surface reconstructions including the c(4 × 4) [54,77,78]. Duszak et al. suggest that work function variations during Ga deposition onto the c(4 × 4) reconstructed surface indicate that Ga can be incorporated in the top layer replacing some As out of the three As dimers. Scanning tunneling spectra indicate the presence of strong Fermi level pinning for the c(4 × 4) surface [79,80].

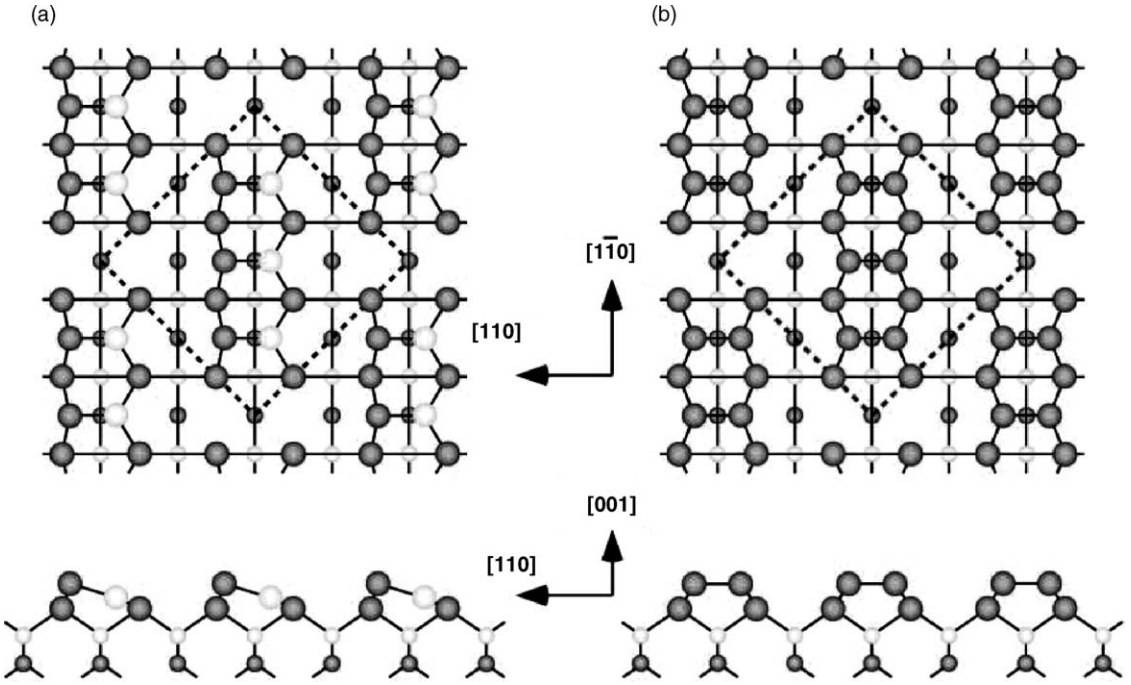

Fig. 12. Top and side views of the α (Ga–As dimer) and β (As–As dimer) structures for the As-stabilized GaAs(0 0 1)-c(4 × 4) surface. Closed (open) circles denote As (Ga) atoms. Reused with permission from [87]. Copyright 2003, American Institute of Physics.

First principles total-energy calculations concluded that the three-dimer model is the energetically most favorable structure under As-rich conditions [81–84]. In addition, the c(4 × 4) structure with only two surface As dimers per unit cell is unstable [85]. Though this structure is more Ga rich than the three As-dimer structure, even in the Ga-rich environment the two-dimer phase has a surface energy that is higher than for the three-dimer phase [85]. These findings along with Biegelsen's observations gave credibility to the three-dimer model which, at that time, had been accepted as the standard model for the c(4 × 4) reconstruction.

Even though the three-dimer model was well-established disagreement still remained as to what causes the wide range of compositions observed for the c(4 × 4) reconstruction. It could obviously not be explained by a three-dimer model with pure As in the first two layers and pure Ga in the third, when the entire surface is perfectly ordered with no As missing from the three As dimers per c(4 × 4) unit cell. The different explanations that have been considered were mostly intermixing of the two species in the second or third atomic layer and a varying number of missing As-dimers in the topmost layer.

Rather recently a new structural model for the GaAs(0 0 1)-c(4 × 4) surface has been proposed which has three Ga–As dimers per c(4 × 4) unit cell [86] (see Fig. 12(a)). The new model is confirmed by a RHEED rocking-curve analysis and first principles calculations as well as a comparison of observed and simulated STM images. Ohtake et al. suggest that two types of structures exist for the GaAs(0 0 1)-c(4 × 4) surface. The c(4 × 4)α with Ga–As heterodimers and the c(4 × 4)β with As–As dimers which corresponds to the formerly accepted standard model (see Fig. 12). The phases are identified by STM, reflectance difference spectroscopy (RDS), and X-ray photoelectron spectroscopy (XPS) [87]. Although

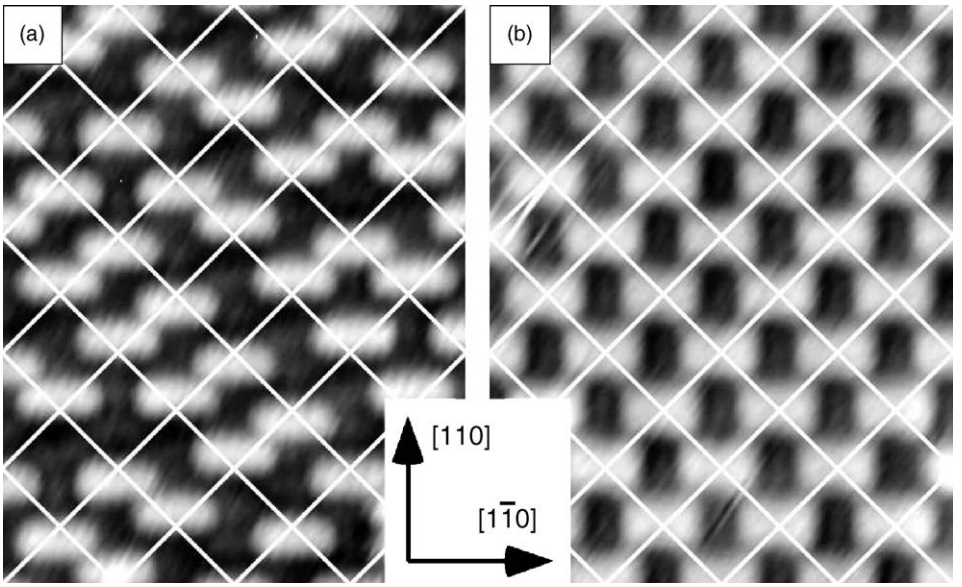

Fig. 13. Filled-state STM images obtained from the GaAs(0 0 1)-c(4 × 4) surface prepared under (a) As_4 and (b) As_2 fluxes. (a) Ga–As dimer structures. (b) As–As dimer structures. Reprinted from [88], Copyright (2004) by the American Physical Society.

similar STM images like those observed by Ohtake et al. had been reported earlier they were interpreted in terms of the three As-dimer model [68]. The α-phase can be obtained by heating the β-phase, while the reverse transition is kinetically limited [87]. A mixture occurs in the transition region. In a later study Ohtake et al. show that depending on the incident As molecular species the α or β structures can be obtained [88]. STM images of both structures are displayed in Fig. 13. Under As_4 fluxes, the c(4 × 4)α reconstruction with Ga–As dimers is obtained, but the formation of three As–As dimer structures is kinetically limited. On the other hand, the structure change from the (2 ×4), through the energetically metastable c(4 × 4)α structure, to the c(4 × 4)β-phase is observed under As_2 fluxes [88]. Ohtake et al. further observed that the three Ga–As dimers in a c(4 × 4)α unit cell are usually aligned in the same direction forming an energetically stable block, while the structure in which one of the dimers is arranged in the opposite direction with others is slightly unstable [89].

Similar RD spectra like those shown by Ohtake et al. for the c(4 × 4)α- and β-phases had been reported earlier for the GaAs(0 0 1)-c(4 × 4) surface, but the interpretation was different [57,90,91]. Kamiya et al., for instance, inferred that the two different observed spectrum features correspond to ordered and disordered c(4 × 4) structures both of which are terminated by As–As dimers [57], without considering the possibility of the formation of Ga–As heterodimers.

Prompted by the recent work of Ohtake et al. Ga–As heterodimers have been considered as structural element in several different studies of the GaAs(0 0 1)-c(4 × 4) surface. Nagashima et al. confirmed that under the conditions of molecular beam epitaxy using As_4, the c(4 × 4) reconstruction on GaAs(0 0 1) has two phases with different surface compositions, which they identify as the α- and β-phases. They present detailed atomic geometries for the two phases [92], which yield significantly better agreement with their experimental data than the twisted As–As dimer model they had proposed earlier [93]. Romanyuk et al. suggest that the twisted As–As dimer model should be valid for the very As-rich surface corresponding to the c(4 × 4)β-phase [94].

Ripalda et al. demonstrated that migration enhanced epitaxy (MEE) of GaAs(0 0 1) can also be utilized to produce the two different types of c(4 × 4) reconstruction (α and β) depending on the As/Ga ratio [95]. Another recent STM study of the initial stage of the transition from the c(4 × 4) to the (2 × 4) reconstruction on MBE grown GaAs(0 0 1) favors models of the c(4 × 4) structure with species intermixing in the first and/or second layer, because the proposed mechanism of a phase-transition-induced Ga atomic jump would be more likely with Ga located in the topmost layers than with pure As [96].

The observation of Ga–As heterodimers by Ohtake et al. has also motivated a number of recent theoretical studies to deal with the structure and the growth processes on the As-rich c(4 × 4)-reconstructed GaAs(0 0 1) surface. By comparing their data obtained from first-principles calculations to several different earlier experimental studies using photoemission and reflectance anisotropy spectroscopy [47,97,98,88,99] Hogan et al. give evidence that the heterodimer model provides the best fit for surfaces obtained by cooling the sample under As_4 flux [100]. Furthermore for c(4 × 4) surfaces obtained with As_2 cooling and As decapping the symmetric dimer model seems to be suitable. Ab initio calculations by Kunsági-Máté et al. show that the growth process on the As-rich c(4 × 4) surface takes place via an As–Ga exchange process in three steps [101]. During the interaction of Ga atoms with the As-rich c(4 × 4) GaAs(0 0 1) surface, the As dimers in the As adsorption layer are first converted into Ga–As heterodimers, then Ga atoms occupy the missing-dimer sites. Eventually, Ga atoms will replace the set of remaining As atoms in the Ga–As heterodimers. This latter process is hindered by an energy barrier, which can explain the fact that stable Ga–As heterodimers have been observed experimentally.

Density-functional theory calculations give evidence that a diversity of atomic structures featuring Ga–As heterodimers exist in a range of stoichiometries, between those of the conventional three As-dimer and the new three Ga–As heterodimer models [25] (see Fig. 14). Heterodimers may be crucial for understanding the (2 × 4)-c(4 × 4)-phase transition, because the diverse combinations of As–As dimers

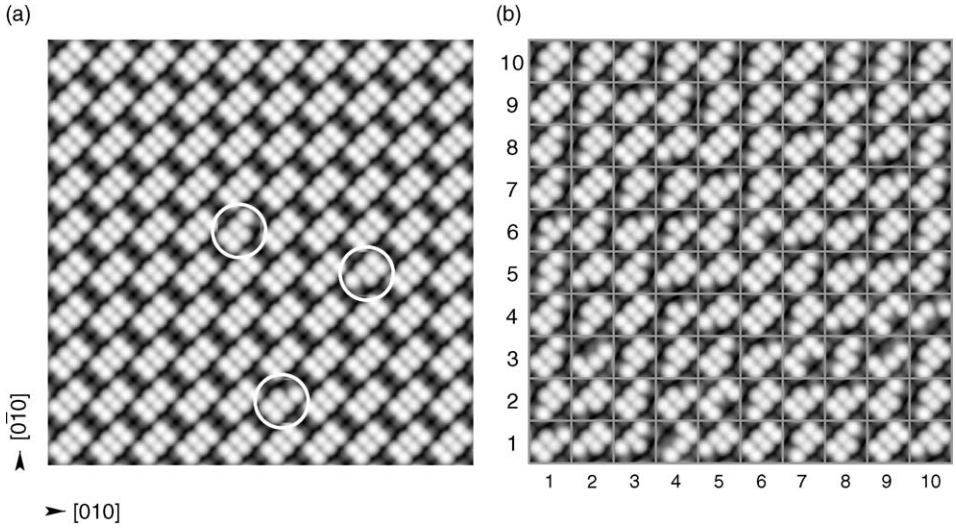

Fig. 14. Simulated filled-state STM images of GaAs(0 0 1)-c(4 × 4) (10 ×10 unit meshes). (a) Nearly perfect conventional c(4 × 4) reconstruction for extreme As-rich limit. (b) Under less As-rich conditions the c(4 × 4) surface reveals a diverse surface with local stoichiometry variations. Reprinted from [25], Copyright (2004) by the American Physical Society.

and Ga–As heterodimers the GaAs(0 0 1)-c(4 × 4) surface features bridges the gap of stoichiometries between the c(4 × 4)α- and β-phases [25]. The motifs Penev et al. show in their simulated filled-state STM images of GaAs(0 0 1)-c(4 × 4) have been observed in several experimental STM studies [63,69,86,87]. (*Note*: replacing one or both of the As atoms in the As dimers with Ga atoms keeps the surface compliant with the electron counting heuristics.)

Using Monte Carlo methods and an ab initio-based approach Ito et al. found that the c(4 × 4)β surface with As–As dimers is stable at temperatures below 400 K, whereas the surface with Ga–As dimers is stabilized at high temperatures in the range 400–700 K [102]. Ito et al. emphasized the important role Ga adatoms play for the epitaxial growth of GaAs on the c(4 × 4) surfaces, because Ga atoms can adsorb and migrate while desorption of As adatoms proceeds without sufficient migration. They also found that three kinds of c(4 × 4) structures consisting of Ga–As dimers and/or Ga–Ga dimers are stable near the phase transition temperature between the c(4 × 4) and (2 × 4)β2 phases [103]. Ishizaki et al. suggested that even a (2 × 4)β2 structure with Ga–As surface dimers may occur in the transition regime evolving from c(4 × 4) units consisting of three Ga–As dimers or one Ga–Ga dimer and two Ga–As dimers. The conventional (2 × 4)β2 surface consisting of As–As dimers finally appears due to destabilization of Ga–As dimers at high temperature and high pressure.

The new structural model including Ga–As heterodimers proposed by Ohtake et al. resolves disagreements in the interpretation of several previous experiments [86]. By including a diversity of atomic structures featuring Ga–As heterodimers between those of the conventional three As-dimer and the new three Ga–As heterodimer models it also provides an explanation for the wide range of stoichiometries that have been observed on GaAs(0 0 1)-c(4 × 4) surfaces [25]. The c(4 × 4)α with Ga–As heterodimers and the c(4 × 4)β with As–As dimers together with diverse combinations of As–As dimers and Ga–As heterodimers in the transition region can be regarded to as the new standard model for the GaAs(0 0 1)-c(4 × 4) surface.

3.2. (2 × 4)/c(2 × 8)

The arsenic terminated GaAs(0 0 1)-(2 × 4)/c(2 × 8) reconstructed surface is often called the "technologically important" reconstruction since it is utilized as the starting surface for growing high-quality GaAs epilayers for commercial optoelectronic devices. The first reported observation of a (2 × 4) reconstruction occurred in 1965 by Jona using LEED on surfaces at room temperature after they were prepared by argon ion bombardment and annealing to about 500 °C under UHV conditions [104]. These LEED experiments were performed after the wafers were quenched to room temperature and self-described as difficult to reproduce. Successful demonstrations of homoepitaxial growth of GaAs under high and ultra-high vacuum came shortly thereafter [2–4]. Their "three-temperature" method was analogous to today's modern MBE method where simultaneous molecular beams of arsenic and gallium impinged upon a GaAs(0 0 1) surface held between 400 and 600 °C under UHV conditions ($<1 \times 10^{-9}$ Torr). Reflected electron diffraction (sic) was employed during growth to determine the crystalline quality of the epilayers. However, reports of surface reconstructions were not given.

Cho was the first to report on the observation of c(2 × 8) and c(8 × 2) surface reconstructions when the substrate temperature was between 400 and 600 °C by performing both reflection high-energy electron diffraction (RHEED) and MBE growth simultaneously [5]. Most significantly, Cho demonstrated that the observed reconstruction is a function of both the substrate temperature and As_2 to Ga ratio in beam equivalent pressures. For example, as the As_2:Ga ratio is lowered from 10 to about 3 the c(2 × 8) pattern

transformed into a c(8 × 2) pattern when the substrate was held at a constant temperature of 570 °C. This observation allowed Cho to correctly surmise that the c(2 × 8) is terminated with arsenic and the c(8 × 2) with gallium. Chang et al. confirmed the presence of the c(2 × 8)-phase with a similar MBE and electron diffraction apparatus. He also confirmed the surface reconstruction's dependence upon the As_2 to Ga BEP ratio and substrate temperature showing for the first time that at low temperatures the c(2 × 8) changed into a c(4 × 4) [40,41].

Arthur was the first to address the question of surface stoichiometry by applying AES, LEED and HEED in situ with MBE of the GaAs(0 0 1) surface [105]. By carefully monitoring the arsenic desorption with temperature it was determined that about one-half a monolayer of As atoms was lost from the surface when it transitions from the As-rich to Ga-rich reconstruction. Using a kinetic model, the relative arsenic content was estimated to be between 0.5 and 0.6 ML for the As-rich surface and <0.1 for the Ga-rich surface.

Using the same in situ RHEED instrument Cho determined that the 2 × periodicity of both the As stabilized (2 × 4) and Ga stabilized 4 × 2 is in the direction parallel to the plane containing the dangling bonds on the surface [42]. He speculated that the 2 ×periodicity was due to dangling-bond-pairing (dimer formation), which was known to be common structural motif on other reconstructed semiconductor surfaces such as Si(0 0 1) [106]. This meant that the As dimers are parallel to the [1 $\bar{1}$ 0] direction and the Ga dimers are parallel to the [$\bar{1}$ $\bar{1}$ 0] direction. He also suggested that another effect was responsible for the 8 × or 4 × symmetry such as surface vacancies and or Fermi surface instabilities [107]. Later on, LEED studies carried out by Van Bommel and Crombeen further confirmed the RHEED evidence of the dimers and their orientation relative to the underlying substrate [108].

Several research groups confirmed the stoichiometry and structural findings by employing electron diffraction, Auger electron spectroscopy (AES), photoemission and EELS [109,43,44]. Massies et al. also performed LEED, CPD, and ELS and confirmed these previous findings that the c(2 × 8) surface was composed of about 0.6 of a monolayer of As [53]. Later on however, Bachrach et al. utilized ARUPS to study the composition of the reconstruction and measured a higher value for the As coverage of 0.89 of a monolayer [46,44].

Larsen et al. proposed the first structural models based on RHEED, ARUPS, and tight binding calculations. The structures they proposed were (2 × 2) unit cells and composed of a full plane of tilted As-dimers [110,111]. They argued that a (2 × 4) or c(2 × 8) electron diffraction pattern could be made up of constructive interface effects from multiple (2 × 2) domains. In addition, the photoemission studies showed that a surface state exists at about 1 eV below the valence band maximum which provided more evidence for As-dimers.

Further theoretical studies by Chadi et al. showed that the formation of As-dimers on and As(0 0 1) surface released about 2 eV per bond, further supporting the fact that the equilibrium (2 × 4) surface is composed of As dimers [55]. The first theoretical effort to study the (2 × 2) reconstructed surface structures using self-consistent pseudopotentials determined that a c(2 × 2) structure is metallic and only a p(2 × 2) with inequivalent As dimers, one buckled one not, would form a semiconducting surface. This was the first evidence that the structural model was more complex than originally surmised. Unfortunately, at the time (1983) computing facilities were not sufficient to fully calculate the density of states for a fully relaxed p(2 × 2) structure [112].

Chiang et al. utilized ARUPS and measured a 0.73 ratio of Ga to As peak intensities for the c(2 × 8) reconstructed surface [48]. In addition Chiang determined that the Fermi level was 0.55 ± 0.1 eV above the VBM by measuring the Fermi-level position of a Au overlayer deposited on the surface. In depth

RHEED analysis by Joyce et al. determined for the first time that the c(2 × 8) and (2 × 4) reconstructions were distinct from one another [113,10]. In other words, the c(2 × 8) reconstruction was made from an out-of-phase arrangement of (2 × 4) unit cells similar to Larsen et al. asymmetric dimer model. It should be noted that in this model a full monolayer of As terminates the surface, resulting in four As dimers per unit cell and a 1:1 ratio of Ga to As in the surface layer, which was inconsistent with previous ARUPS studies [53,48]. Later, Larsen et al. looked at dynamic effects of RHEED and determined that the RHEED data could not be explained by a purely kinematical calculation of the known surface structures, but required a full dynamical calculation based on a realistic surface model [114].

The first theoretical and experimental evidence for a GaAs(0 0 1)-(2 × 4) structural model that was consistent with previous structural and stoichiometric findings occurred simultaneously in 1987 by Chadi and Frankel et al., respectively [115,116]. Chadi determined from tight binding calculations that the lowest-energy, non-metallic equilibrium surface structures were composed of *missing As dimers* in agreement with Cho's earlier speculation of surface vacancies and was consistent with previous stoichiometry measurements of less As than Ga in the top surface layer [115]. There were two non-metallic missing-dimer models proposed which had the lowest formation energy to within ±0.02 eV of each other which are shown in Fig. 15. The first model, now known as the β2 consists of two As dimers and a third As-dimer a monolayer below in a trench shifted out of phase with the top two dimers shown in Fig. 15(c). The second model, now known as the β consist of three As dimers in a row and then one missing As-dimer shown in Fig. 15(b). Both models have an As coverage of 0.75 ML (including the subsurface dimer in the β2) and only three As dimers per unit cell or a 4:3 Ga:As ratio which satisfies the electron counting model.

Frankel et al. experimental HREELS studies of the vibrational spectra of chemisorbed H on this surface measured an intensity ratio R from 1.5 to 1.0 for the As–H stretching mode to that of the Ga–H stretching mode [116]. The surfaces were prepared ex situ and capped with As which was later removed in the HREELS chamber by heating the surface. Several structures were observed with LEED and the most As-rich c(2 × 8) structure observed had $R = 1.5$. This result indicated that some Ga must be exposed on the arsenic-rich surface indicating that the surface had less than a full monolayer of As which was consistent with previous stoichiometry measurements. Using the intensity ratio of 1.5 they

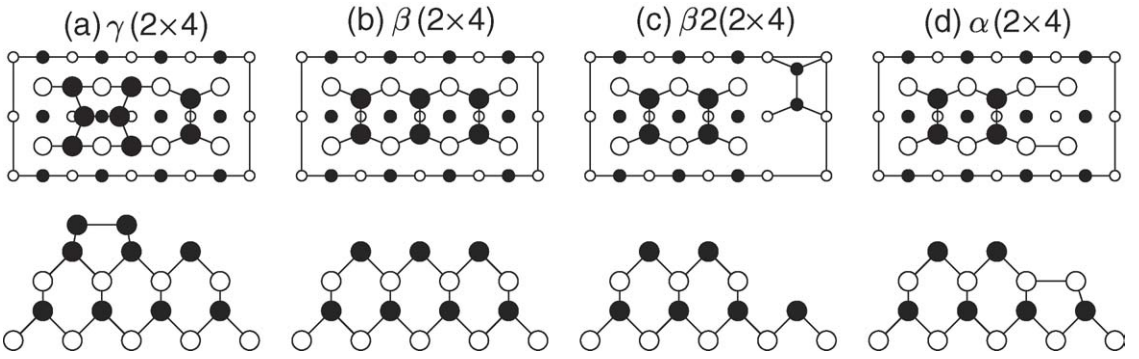

Fig. 15. Four proposed structural models of the GaAs(0 0 1)-(2 × 4) surface reconstruction. Each model shows two views, top (above) and side (below), and the names given to the structural model is indicated in the figure. Filled and empty circles represent As and Ga, respectively. Larger circles represent atoms closer to the surface. Reprinted from [117], Copyright (1999) by the American Physical Society.

speculated that the ratio of exposed Ga to As was also 1.5, or the surface had four Ga atoms exposed for every six As atoms. Three missing As-dimer models were independently proposed that were similar to Chadi's. The first was the three-dimer β model, the second now known as the α model was a two-dimer model similar to Chadi's β2 but with extra Ga in the trench. The third, now called the γ model had an extra As-dimer on top of the surface rotated by 90°.

In a combined experimental and theoretical study Larsen and Chadi reconciled the new missing-dimer structures with the old buckled asymmetric-dimer models [118]. Results from LEED, RHEED, ARUPS, and total energy calculations were compared and it was concluded that: (1) the surface is measured to be non-metallic using photoemission, (2) models with a full monolayer of As and either symmetric or asymmetric dimers are found to be metallic and thus *inadequate*, (3) structures composed of 0.5 or 0.75 ML of As have the lowest energy and are non-metallic, (4) the three-dimer β model with 0.75 ML of As gives the best general agreement with the photoemission data. A note was added in proof that said that the proposed structures were in good agreement with the first soon-to-be-published STM images of this surface. In a follow up paper, density functional theory calculations for (1 × 1) and (2 × 2) surfaces that took into account the appropriate chemical potential of the species showed: (1) dimerization of As lowered the energy by up to 1.7 eV, (2) asymmetric dimers were higher in energy than symmetric ones. In addition, tight binding approach was utilized for the larger (2 × 4) structures and showed that a (2 × 4) surface is only stable with less than a monolayer of As and more stable than a (2 × 2) because of orbital rehybridization effects which are not possible in the smaller cells [119].

The first ultra-high vacuum STM studies were performed by Pashley et al. on GaAs(0 0 1) surfaces prepared ex situ and capped with arsenic [120]. The arsenic was then thermally removed in the UHV STM chamber and images were acquired that showed direct evidence of the missing row structures proposed by Chadi and Frankel. The images showed a large amount of disorder, kinks, and mixed (2 × 4) and c(2 × 8) domains which made it challenging to discern which of the four proposed missing-dimer models was present on the surface. The first in situ UHV STM study came shortly thereafter which produced more well-ordered and uniform surfaces that also confirmed the missing row structures, observed mixed (2 × 4) and c(2 × 8) domains, and observed structures consistent with the three arsenic dimer models [121,60]. The authors noted that two-dimer structures could be observed if the surface was annealed to higher temperatures.

These initial STM studies made it clear that well-ordered (2 × 4) surfaces had missing arsenic dimers. However preparing a well-ordered surface was challenging and very sensitive to the preparation conditions. The most notable work to demonstrate that the structure of the (2 × 4) unit cell may undergo a transformation due to changes in the arsenic flux and substrate temperature was by Farrell and Palmstrøm [122]. By monitoring changes in the intensities of the quarter-order spots of the [$\bar{1}$ 1 0] (4×) RHEED pattern they were able to identify three distinct phases and named them α, β, and γ (cf. Fig. 2). These phases corresponded to a decrease in temperature at a constant arsenic flux. Using kinematic diffraction theory they predicted three distinct (2 × 4) structural models as the origin of these different patterns. These models were correspondingly called the α, β, and γ models as discussed previously and shown in Fig. 15. These predictions, though plausible, were never confirmed by STM, LEED, or first principles density functional theory. However, the three phases are clearly discernable in RHEED and they did have a significant impact on all future investigations. In addition, it was the first use of Greek letters to identify the structural models.

Numerous other in situ STM and diffraction studies appeared that all confirmed the presence of structures consistent with the missing-dimer models [61,123–127,54,128–135]. However, there was

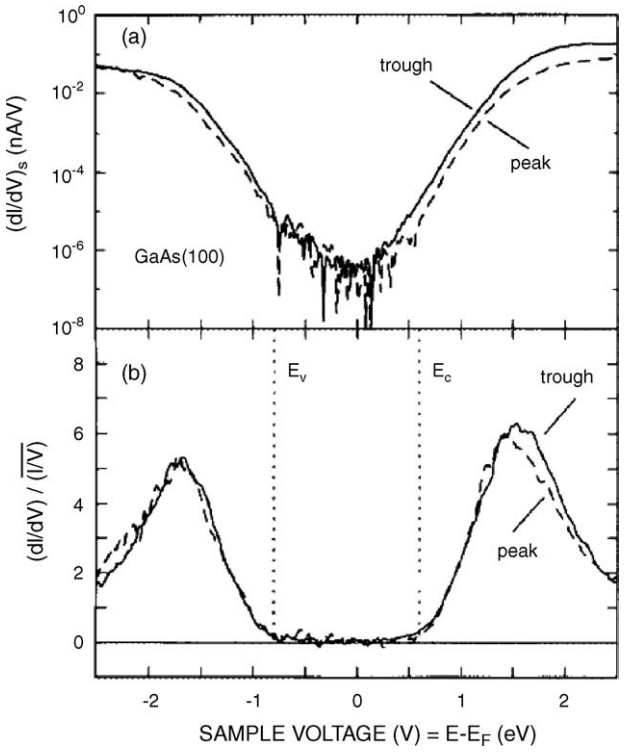

Fig. 16. Comparison of STS spectra of the GaAs(0 0 1)-(2 × 4) surface acquired from top As-dimers (peak) to the trench (trough) between the dimer rows. The spectra show the Fermi level is pinned near mid gap. Reprinted with permission from Pashley et al. [123]. Copyright 1992, AVS The Science and Technology Society.

discrepancy in the reports for which of the four missing-dimer models was actually observed. In addition, it became clear that this surface was sensitive to preparation conditions. For example, an in situ MBE and STM study confirmed missing-dimer structure and possibly the three-dimer β model [61]. Soon after another in situ STM study showed a very well-ordered (2 × 4) reconstructed surface with only two dimers in the outer most layer consistent with the α or β2 [123,124]. This study also showed that Si doping of the GaAs substrate increased the observed step kink density. Spatially resolved STS was performed and showed that negative charge is located at the kinks and they act as acceptors and are occupied by one electron, while the Fermi level is found to be pinned near mid gap for the rest of the surface as displayed in Fig. 16 [123,124]. In a follow up study it was determined that p-type (10^{19} cm^{-3} Be) doped substrates did not have similar surface donor states near the kinks [130]. In addition, the Fermi level was found to be 150 meV above the VBM and moves mid gap with a decrease in the Be doping. An in situ STM and STS study confirmed the presence of only two top As dimers [127]. STS confirmed that the Fermi level was pinned near mid-gap and that it was difficult to access the unoccupied states of the surface which was attributed to tip induced band bending.

The first study to address Farrel and Palmstrøm's (2 × 4) sub-phase scheme was a combined work function, LEED, RHEED, and STM study on As capped then desorbed surfaces [54]. It was noted that surfaces prepared in the β-phase had the highest work function [0.82 eV greater than the (1 × 6)] and were the most well ordered. Interestingly, the authors reported that they could *n*ot observe the α-, β-, or γ-

phases using LEED as in RHEED. Photoionization measurements had a maximum in the β-phase and was explained in terms of a change in surface dipole [129].

In situ MBE STM comparison of MBE grown and Ar ion bombarded surfaces showed that MBE produced a more well-ordered surface. The three-dimer β model was presumed to match the image the best. The Ar-ion bombarded surfaces showed more disorder with difficulty in discerning the unit cell, but rows due to missing dimers could be observed [131,132]. An in situ MBE STM and field ion microscopy study also confirmed the presence of missing As dimers of the (2×4) unit cell with no further indication of which structure was being observed [133]. A RHEED rocking curve measurement of this surface agreed well with elastic multiple-scattering (dynamical) theory of the three-dimer β model [135].

In the early 1990s computing facilities were getting powerful enough to perform total energy calculations of the (2×4) structural models. For example, modeling only the top monolayer of the β model requires only 14 atoms. However, at least eight bulk layers of GaAs terminated with pseudo-hydrogen atoms are required to model these structures, increasing the number to about 100 atoms. In 1993 Ohno published the first total energy calculations within the local density approximation of a fully relaxed (2×4) structure determined that a complete monolayer of As is unstable and that structures of missing dimers are the only stable structures. The formation energy versus arsenic chemical potential was calculated using six bulk layers underneath the reconstruction and showed that the $(2 \times 4)\beta$ structure was 0.02 eV/(1×1) lower in formation energy than the β2 structure and these were the lowest two structures of six that were studied that included the four proposed initially by Chadi and Frankel [136].

Shortly thereafter, Northrup et al. demonstrated using first principles DFT-LDA studies of only the γ, β, α structures using up to 12 slab layers that the β model was the lowest energy structure over the broadest range of chemical potential. In addition, the γ model was found to be energetically unfavorable and at higher chemical potentials the α model was favorable [82]. A follow up study by Northrup et al. that included the β2 structure showed that the β2 was 0.05 eV/(1×1) *lower* in formation energy than the β, which contradicted Ohno's previous finding [81]. In addition, this reduction closed the chemical potential window for the α model, making unlikely that it could be observed. It was explained that the lower formation energy for the β2 arose from a reduction in the Madelung (electrostatic) energy between the two As dimers when compared to the three As dimers of the β model.

To compare to STM images, surfaces of constant charge density were extracted from first principles DFT-LDA calculations of the $(2 \times 4)\beta$ structure [137]. These surfaces showed three distinct lobed features of equal height for the filled states, one lobe for each As dimer. Shortly thereafter, ab initio pseudopotential methods were used to study the β2 model and determined that there were two different Ga–As bond lengths between the first and second layer due to the hybridization of the Ga atoms in the second layer. The Ga in between the two As dimers remain sp^3 hybridized similar to the bulk, where as the Ga atoms on the outside of the dimers rehybridize from sp^3 to sp^2 [138].

In 1996 four independent first principles DFT calculations of seven different (2×4) structural models for GaAs(0 0 1) surface all showed that the β2 structure had the lowest formation energy over the range in chemical potential for which the (2×4) reconstruction is favorable [83,85,139,140]. Three studies computed the formation energy of the β2 to be 0.01 eV/(1×1) [83], 0.045 eV/(1×1) [139], and 0.05 eV/(1×1) [140] lower than the β structure. In addition to DFT-LDA, Zhang and Zunger used a linear combination of structural motifs (LCSM) technique that showed the β2 model had the lowest formation energy by 0.08 eV/(1×1) [140]. Recently, a new α2 model has been proposed that is similar to the α model but with one missing top layer As-dimer [141]. Total energy calculations of this model have determined it to have a lower formation energy than the α model, but not more stable than the β2

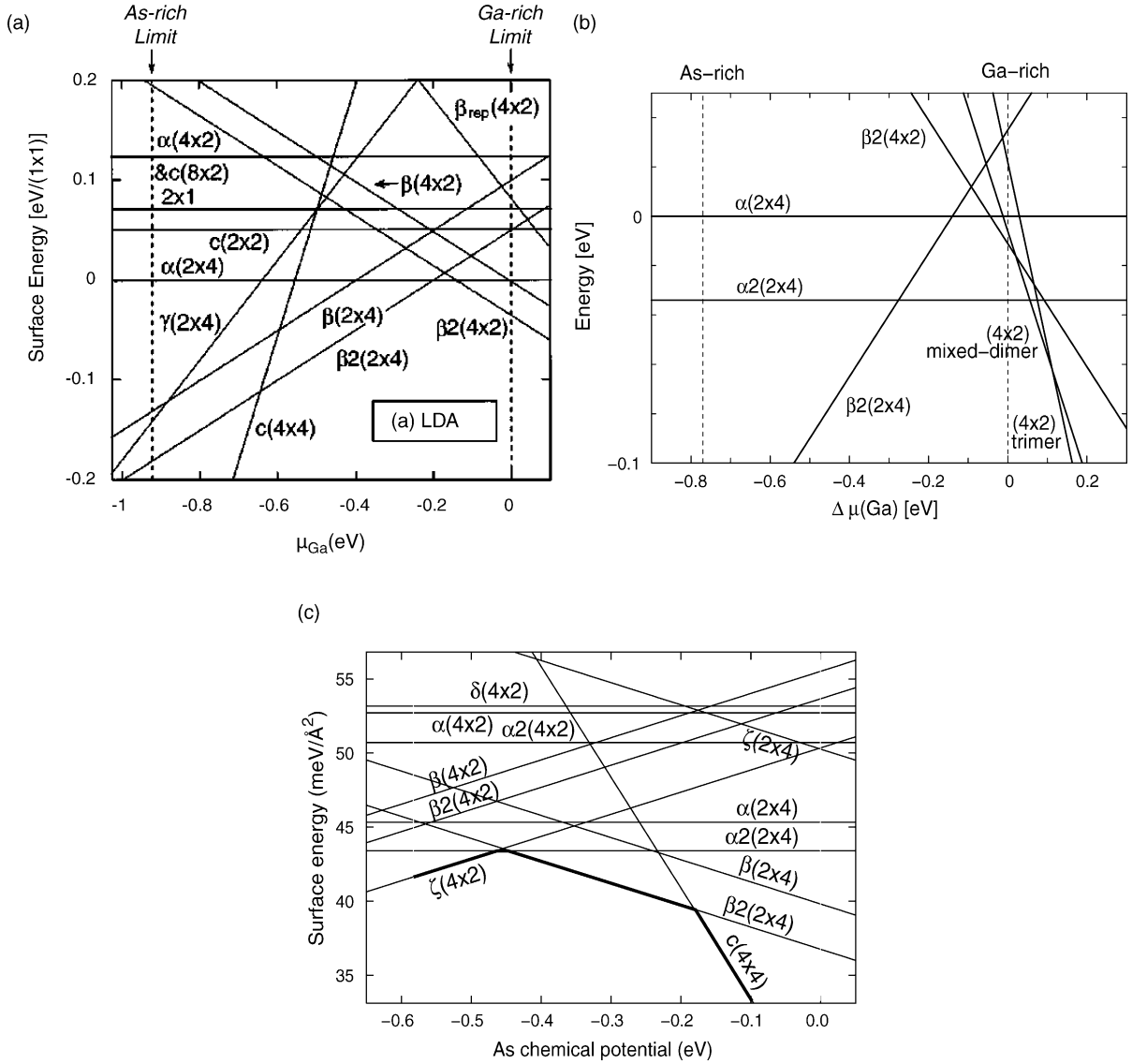

Fig. 17. Three independently computed phase diagrams which plot the relative surface energy vs. anion or cation chemical potential as indicated. These three plots indicate that the β2 model is the lowest energy (2 × 4) structure over the broadest range in chemical potential. Reprinted from: (a) [140], Copyright (1996) by the American Physical Society, (b) [141], Copyright (2000) by the American Physical Society and (c) [142], Copyright (2000) by the American Physical Society.

model [141,142]. Theoretically calculated phase diagrams of formation energy versus cation or anion chemical potential for each reconstruction model from three research groups are displayed in Fig. 17. The diagrams clearly indicate that the α model has a very narrow (or even non-existent) chemical potential window just before the surface transforms to the Ga-rich (4 × 2), making it unlikely that the α structure could be observed. The coordinates of the fully relaxed structures for the α, β and β2 models as computed using DFT-LDA by Schmidt and Bechstedt are displayed in Table 1 and Fig. 18 [139].

Table 1
Geometrical parameters in Å of the relaxed GaAs(0 0 1)-(2 × 4) α, β2, and β structures according to Fig. 18

GaAs(0 0 1)-(2 × 4)	α	β2	β
$\Delta_{a1,x}$	2.50	2.50	2.50
$\Delta_{a2,x}$	2.50	–	2.50
$\Delta_{b1,x}$	3.85	3.65	3.65
$\Delta_{b2,x}$	3.64	3.52	3.49
$\Delta_{b3,x}$	3.50	–	–
$\Delta_{b4,x}$	3.66	–	–
$\Delta_{c,x}$	–	2.52	–
$\Delta_{d,x}$	–	3.70	–
$\Delta_{a,y}$	3.92	3.82	3.80
$\Delta_{b,y}$	2.50	–	–
$d_{ab,y}$	1.50	1.41	1.42
$d_{ab',y}$	1.73	1.44	–
$d_{ac,y}$	–	5.92	–
$\Delta_{a,\perp}$	0.06	–	0.02
$\Delta_{b12,\perp}$	0.20	0.28	0.24
$\Delta_{b23,\perp}$	0.19	–	–
$\Delta_{b34,\perp}$	0.22	–	–
$d_{ab,\perp}$	1.42	1.49	1.47

Reprinted from [139], Copyright (1996) by the American Physical Society.

Motivated by the three phase scheme of Farrel and Palmstrøm, Hashizume et al. prepared three surfaces in each of the three phases and imaged them in situ with STM [62,65,143,13,12]. All three STM images clearly showed the presence of only two dimers and two dimer vacancies per unit cell. The only observable difference was the amount of long-range disorder in the form of kinks or unit cell vacancies that both the α and γ surfaces had over the β surface which was the most well ordered. Dynamical RHEED calculations were also performed that showed: (1) the three-dimer β model and the γ model could not account for any of the observed RHEED patterns, (2) the calculated RHEED pattern from the β2 model agreed best with the β-phase RHEED pattern, (3) the calculated RHEED pattern from the α model agreed best with the α-phase RHEED pattern, and (4) the γ-phase RHEED pattern did not have any structural model associated with it. They used these results to conclude that the surface is the α structural model when in the α-phase and the β2 structural model when in the β-phase and the γ-phase RHEED pattern was due to disorder as the surface changed reconstruction from the (2 × 4) to c(4 × 4) reconstruction. Height cross-section from the three STM images all showed only a 2.1 Å deep trench which was 0.7 Å smaller than what would be expected for the β2 model which was attributed it to a tip effect.

Another in situ STM study the α-, β-, and γ-phases that seemed to contradict Hashizume et al. previous finding observed images of four distinct (2 × 4) structural models [144]. The three-dimer β model was observed in the β-phase contradicting Hashizume et al. previous finding. Both the two-dimer β2 model (called α1) and the α model (called α2) were observed in the α-phase. The image acquired in the γ-phase could not be explained by any previously reported model. The height differences measured from the top As-dimers to the trench was only 1.3 Å, which was 1.5 Å smaller than expected and was attributed to variations in the surface charge density [144].

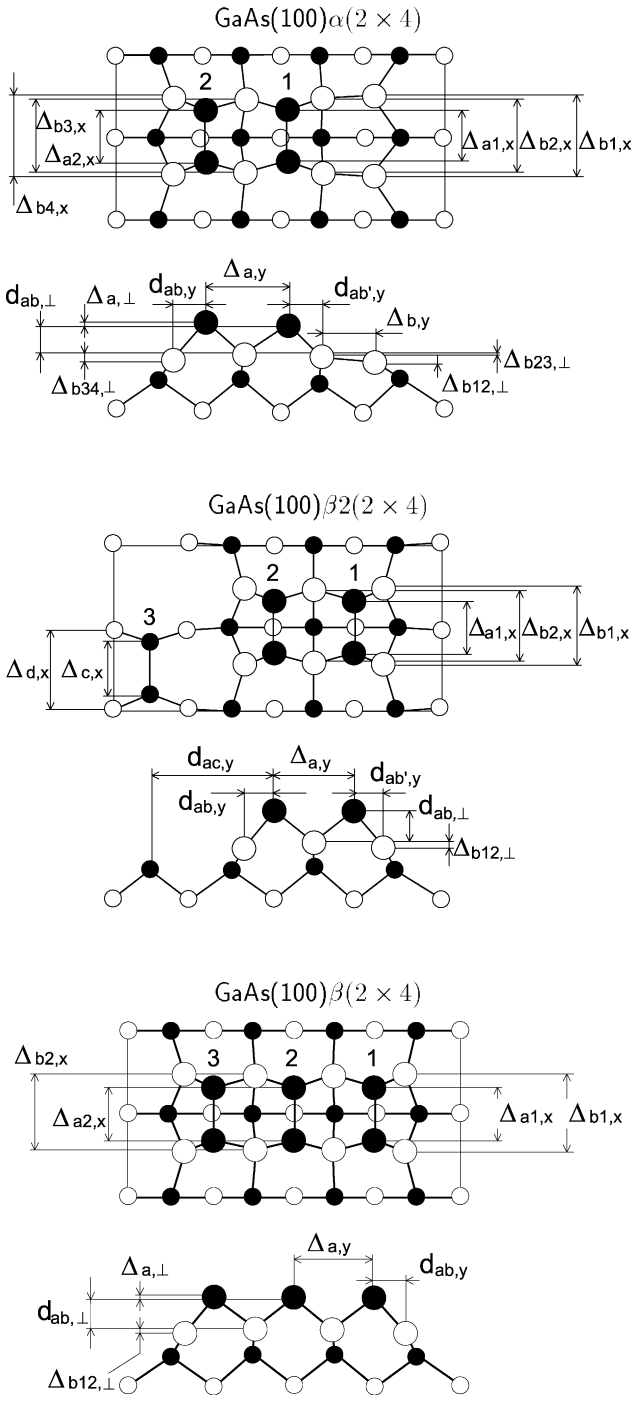

Fig. 18. Top and side view of the relaxed GaAs(0 0 1)-(2 × 4) α-, β2- and β-phases. Large (small) filled circles indicate top (third) layer As atom whereas large (small) empty circles represent second (fourth) layer Ga atoms. Reprinted from [139], Copyright (1996) by the American Physical Society.

More in situ STM studies appeared that all confirmed that the top surface layer was composed of only two dimers which was consistent with both the α or β2 models [145,63,146]. Based on STM observations and tight binding calculations of the γ-phase, Avery et al. concluded that the disorder in the γ-phase arose from kink formation from the preferential occupation of second layer Ga sites by additional As atoms in the missing-dimer trenches of the β2 structure. It was determined that the kinks did not arise from doping effects as observed previously by Pashley et al. Rather, when the kink forms, it is energetically more favorable to have As atoms occupy the second layer Ga sites [123,124]. Recent X-ray diffraction studies have shown that a characteristic motif of the gamma phase are trenches with a width of seven surface lattice constants, and most likely As dimers on an As layer sit in these trenches [147]. These studies provide some explanation for why the γ-phase has a higher As coverage than the β-phase.

Grazing incidence X-ray diffraction measurements of the most well-ordered (2×4)- β-phase were in agreement with the β2 model. [148]. Reanalysis of dynamical RHEED intensity and rocking curve data by McCoy et al. showed that the most well-ordered surface is the two-dimer β2 model not β as was previously determined [149,135]. Reflectance anisotropy spectroscopy (RAS) and tight-binding theory of the various arsenic-rich (2×4) phases agreed well with the β2 structure for the β-phase and the α structure for the α-phase [66].

At this time confusion still existed (α or β2) as to the exact structure of the this surface for researchers who were studying submonolayer heteroepitaxial growth on this surface [150,151]. Even though theoretical methods and diffraction techniques pointed to the β2 structure as the correct model, conclusive proof by STM of the structure within the trenches of the (2×4) surface was not available.

In 1999 LaBella et al. acquired several STM images as a function of STM tip bias that resolved all the atomic features of the well-ordered β-phase surface. The features were in excellent agreement with first principles density functional theory of the β2 structural model [117]. A filled-state STM image of the GaAs(0 0 1)-(2×4) reconstructed surface taken with a sample bias of -2.1 V is shown in Fig. 19(a). The multiple bright rows, running diagonally across the image, have a center-to-center distance of 1.6 nm along the [1 1 0] direction, representing the ''4-by'' periodicity of the (2×4) reconstruction. Along the [1 $\bar{1}$ 0] direction another oscillation in the gray level occurs at twice the spatial frequency or every 0.8 nm representing the ''2-by'' periodicity of the (2×4) reconstruction. These ''2-by'' features are topographically flat and have an overall width of $\sim$0.9 nm along the [1 1 0] direction. They indicate that the top layer structure consists of two dimers of equal height as depicted by the two ball-and-stick dimer models drawn over the STM image in Fig. 19(a). This is inconsistent with the γ model [cf. Fig. 15(a)] which would have an additional As dimer on top of the row. It is also inconsistent with the β model [cf. Fig. 15(b)] which would have a feature spanning over $\frac{3}{4}$ of the length of the ''4-by'' width.

The structure within the trenches between the top layer As-dimer rows is also resolved in Fig. 19(a). The periodicity of the trench structure is 0.8 nm along the [1 $\bar{1}$ 0] direction, similar to the ''2-by'' periodicity of the top layer dimer rows. However, this trench periodicity is shifted out of phase with the ''2-by'' periodicity of the top layer dimer rows, indicated by the white line and the three ball-and-stick As dimers drawn over the data. This shift is inconsistent with the α model, which has a symmetric arrangement of atomic features between the trenches and the top layer [cf. Fig. 15(c)]. This shift and all the other observed features in Fig. 19(a) are in agreement with the β2 model [cf. Fig. 15(d)].

First-principles generated STM images of the β2(2×4) structural model at a filled-state bias of 0.3 V below the VBM are displayed in Fig. 19(b) as a continuation of the STM data shown in Fig. 19(a). The images were extracted from density functional calculations without modeling the STM tip. These

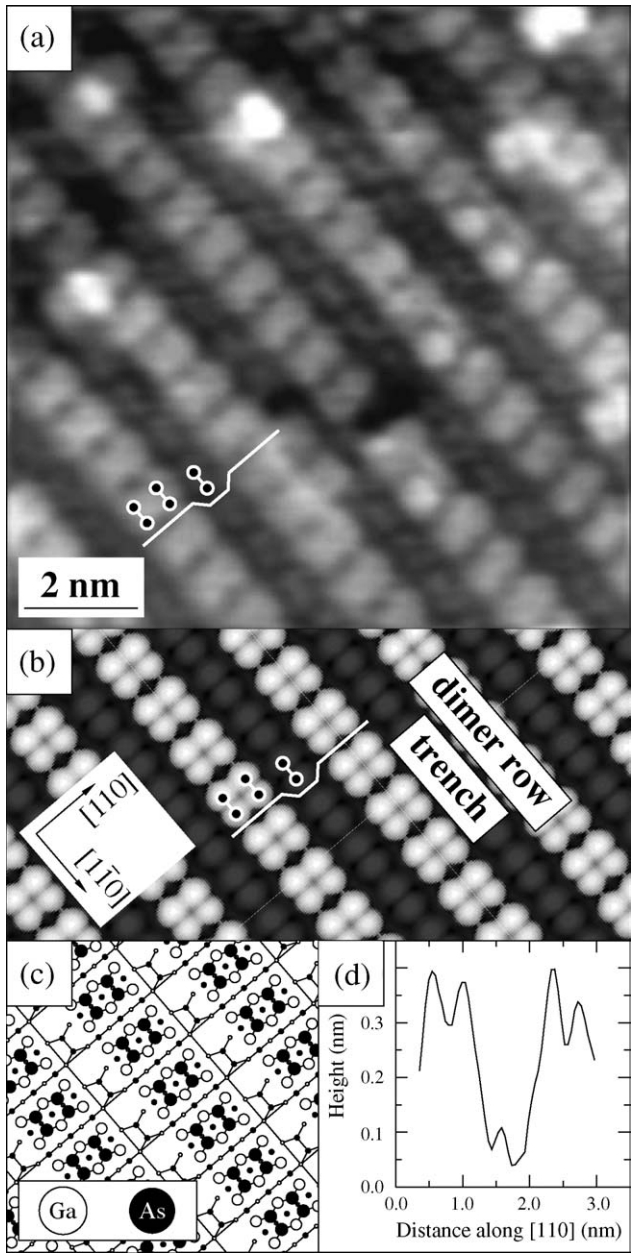

Fig. 19. (a) Filled-state STM image acquired with a sample bias of −2.1 V measuring 11 nm × 11 nm; (b) simulated STM image of the β2 structural model using a filled-state bias of 0.3 V below the valence band maximum; (c) β2 structural model; (d) height cross-section across a dimer trench along the [1 1 0] direction extracted from the STM image shown in (a). Reprinted from [117], Copyright (1999) by the American Physical Society.

calculations were performed within the local-density approximation by employing a plane-wave-pseudopotential approach with a cutoff energy of 10 Ryd [152]. The GaAs(0 0 1) surface was modeled as a seven-layer slab followed by a vacuum region larger than 2 nm. The bottom layer of atoms was passivated with pseudo-hydrogen atoms and kept fixed, while the top six layers were relaxed until all the forces were less than 0.5 eV/nm. After structural relaxation, extracting isocontour surfaces of a suitably defined local density of states generated numerically simulated constant current STM images. The local density of valence band states were integrated from the valence band minimum (VBM) to 0.3 and 1.1 eV below the VBM. This mimics the range of filled-state sample biases used in the STM images, which are referenced with respect to the Fermi level of the sample located in the middle of the 1.4 eV surface band gap [130].

A height cross-section taken along the [1 1 0] direction from the STM data displayed in Fig. 19(a) is shown as a line scan in Fig. 19(d). This height cross-section spans two top-layer dimer rows and the trench between them. This line scan shows that the topographic depth change that occurs between the dimer rows is ~ 0.3 nm, or a full monolayer (ML) height for GaAs(0 0 1). This is in agreement with the $\beta 2$ model [cf. Fig. 15(c)] and in disagreement with the α model, which would show a height difference of only half a monolayer (0.14 nm) [cf. Fig. 15(d)].

The features seen in the STM data and the agreement with the density functional theory conclusively point to the $\beta 2$ model as the correct structural model for this surface. Interestingly, however, the trench structure could only be resolved at the low sample biases as demonstrated in the nine (11 nm $\times$ 11 nm) STM images shown in Fig. 20. These images are of the same region of the GaAs(0 0 1)-(2 $\times$ 4) reconstructed surface and were taken at biases ranging from -3.0 to -2.1 V as indicated. The location of the same feature in all the images is indicated by the white circle. Visible in these images are the top level As-dimer rows running diagonally in the [1 $\bar{1}$ 0] direction. In addition, the structure within the trenches first becomes visible when the sample bias is between -2.6 and -2.4 V. The best visibility is from -2.3 to -2.1 V.

To better illuminate the differences in the bias-dependent images a 2.8 nm $\times$4.4 nm section of the same region taken from both the -3.0 V bias image and -2.1 V bias image are shown in Fig. 21. The internal structure of the top layer ''2-by'' features is better resolved at the -3.0 V bias image. Namely, a distinct single minimum exists at the center of the top layer dimer row, indicating the presence of only two As dimers in the top layer and further supporting the $\beta 2$ model. This single minimum is less pronounced in the image taken of the same region but with a smaller sample bias of -2.1 V shown in Fig 21(b). Most significantly, this smaller-bias STM image reveals the atomic structure within the trenches.

A bias-dependent feature in an STM image typically results from variations in the local density of states (LDOS) of the surface [153]. However, under filled state tunneling conditions, changing the tip bias does not alter the energetic window from which electrons are extracted from the sample, since the tunneling probability always has a maximum at the valence band maximum. Therefore, changing the tip bias would not alter the tunneling probability as it does for empty state tunneling. This indicates that the observed change cannot be explained by a change in the LDOS of the surface.

The mechanism that explains this bias-dependent difference in the STM images was discovered after bias-dependent simulated STM images were produced. The simulated STM images taken at filled-state biases of 1.1 and 0.3 V below the VBM are shown rendered in three-dimensions in Fig. 21(c) and (d), respectively. These images reveal a mammoth 0.3 nm increase in the physical width of the trench region as the filled-state bias is reduced by 0.8 V. This increase is monotonic, and is consistent with the monotonic change in the bias-dependent STM images. The trench widens as a result of the retracting surface of constant LDOS about the top layer As-dimer dangling bond orbital. This retraction allows the

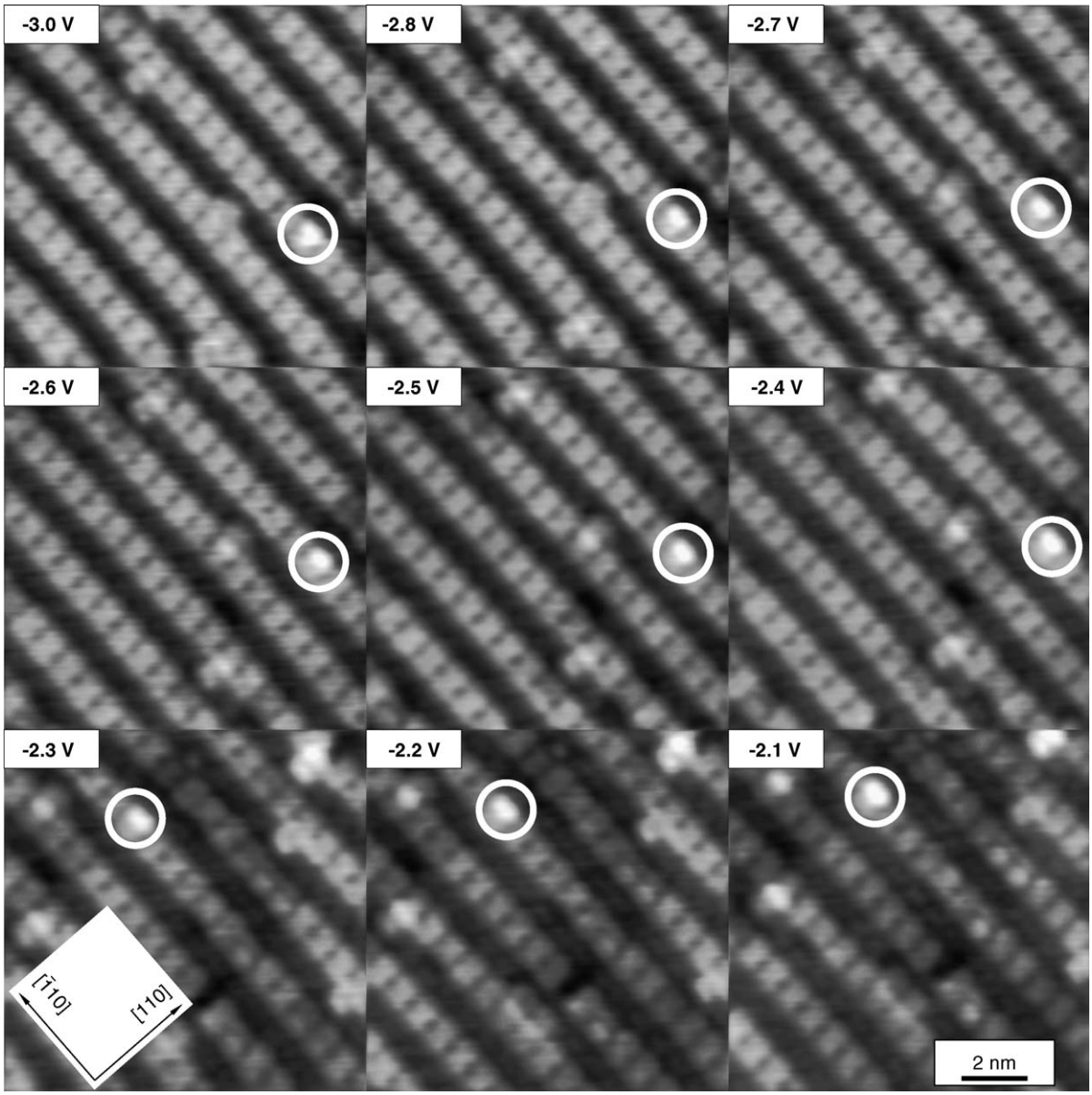

Fig. 20. Nine filled state STM images of the same measuring 11 nm × 11 nm region of the GaAs(0 0 1)-(2 × 4) reconstructed surface. Sample biases range from −3.0 to −2.1 V as indicated. Reprinted with permission from [31], Copyright (2001) World Scientific.

STM tip to penetrate between the top-layer As dimer rows and image the As dimers within the trenches that are a monolayer (0.28 nm) lower. At larger biases, the narrower trench results in the tunneling current jumping from one top-layer As dimer to the next, missing the features in between. Thus, even though the As dimers within the trench have a uniform LDOS, at high biases those states are blocked by the orbitals of the top-layer As dimers.

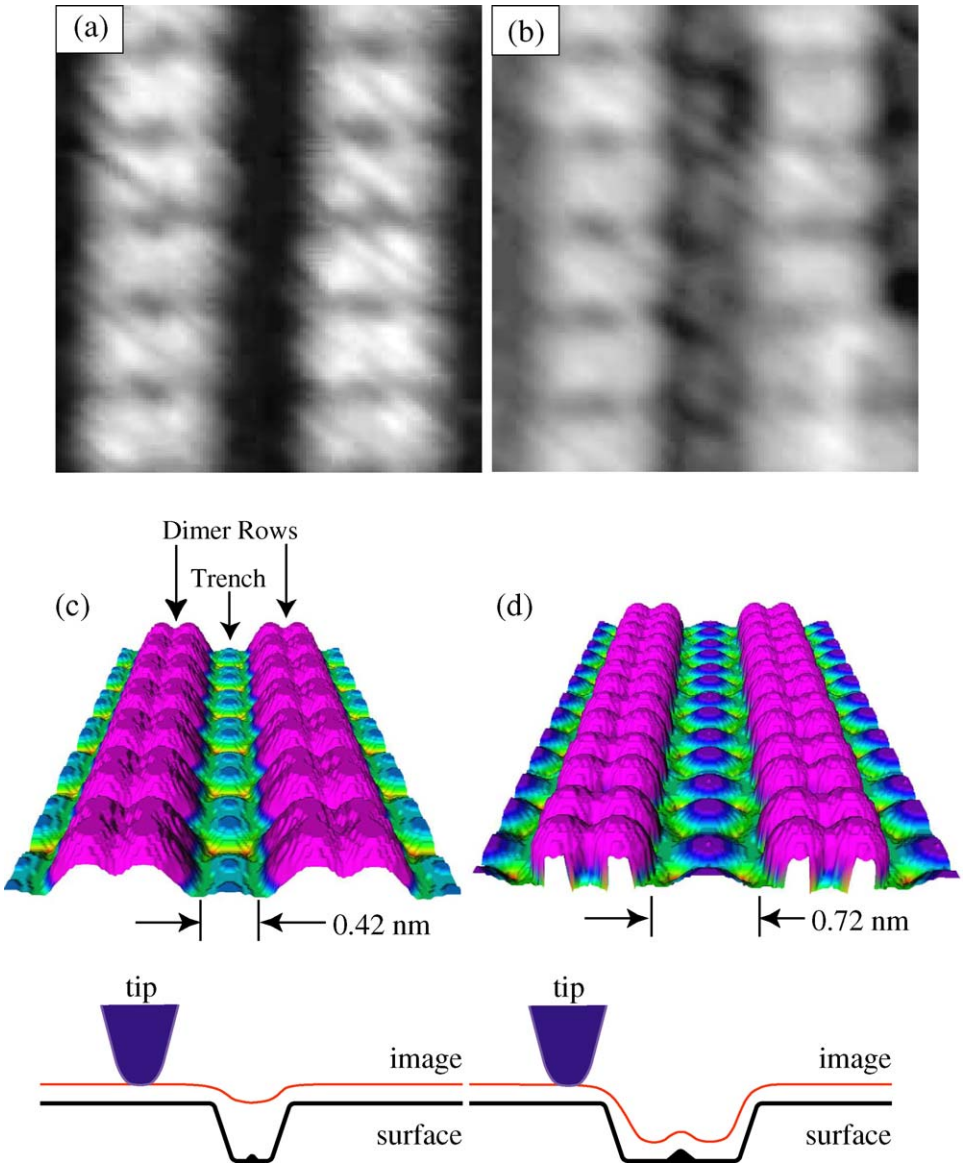

Fig. 21. (a) and (b) 2.8 nm×4.4 nm filled-state STM images of the same area acquired with sample biases of −3.0 and −2.1 V, respectively. (c) and (d) Simulated STM images using a filled-state biases of 1.1 and 0.3 V below the valence band maximum, respectively. Reprinted with permission from [31], Copyright (2001) World Scientific.

An apt analogy for explaining the inability to image features within the trenches at larger biases is a geometric sample–tip convolution effect commonly seen in scanning probe microscopy [154]. However, geometric convolution effects do not disappear as the bias is lowered. In addition, they typically happen on length scales which are at least an order of magnitude or more larger than the 0.3 nm observed here. This new phenomenon was described as an electronic sample–tip convolution effect. In this phenomenon, the step edge of the trench is sharper at smaller biases, and this electronic sample sharpening

reduces the geometric tip–sample convolution, allowing the finite size tip to image inside the trench. This is a novel contrast mechanism and illustrated in the lower portion of Fig. 21. Since this observation the ''sample sharpening'' mechanism has also been observed on InAs(0 0 1)-(2 × 4) surface [155]. In addition, analysis of RHEED rocking curve and reflectance difference spectroscopy (RD) spectra data of the α-, β-, and γ-phases concluded that the α-phase has the same β2 structure as the β-phase but with slightly different atomic coordinates [156].

In summary, all the atomic features of the well-ordered GaAs(0 0 1)-(2 × 4) reconstructed surface have been resolved and conclusively point to the β2 model as the correct model. It is now believed that the β2 model spans the entire (2 × 4) regime. Spontaneous island formation or roughening was found to coincide with the onset of the α-phase RHEED pattern and will be discussed in the next section.

4. Roughening and spontaneous island formation

Surfaces roughen to lower their free energy at high temperatures. Surface roughening has been well studied both theoretically and experimentally especially for metal surfaces that have no reconstruction or reconstructions with a small number of atoms per unit cell when compared to semiconductors [157–159]. At temperatures below the roughening temperature, T_r a flat surface is favorable and as the surface is heated through T_r it undergoes a phase transition to a rough surface with long wavelength variations in the height where the energy cost to form a step, or step free energy has vanished [158,160,161]. The roughening temperature has important consequences for crystal growth. Below T_r, growth is mediated by island nucleation an activated processes that depends upon adatom diffusion and nucleation energies. Above T_r, crystal growth proceeds in a continuous fashion that is a function of the chemical potential difference across the vapor–solid interface.

The surface transformation that accompanies the change in RHEED patterns from the flat well-ordered (2 × 4)- β-phase through the (2 × 4)- α-phase to the (2 × 1) phase is a roughening transition [162,31,18,163–166]. However, this understanding has only come about very recently due in part to lack of accurate and reproducible temperature control and the driven searches to uncover the atomic structure of the various reconstructions that ignore larger nanoscale structures such as island formation that occur during roughening. This section will review the theoretical models needed to understand this roughening transition and the recent experimental evidence.

4.1. Theoretical models of surface roughening

Macroscopic thermodynamic continuum models and microscopic ''broken-bond'' lattice models are two approaches to model roughening. 2D microscopic atomistic models have a large appeal today in part due to the ability to measure the real space configuration of a rough surface on the atomic scale with STM and their ability to be readily simulated using modest computational facilities. These 2D many body models belong to a larger class of 2D many body models analyzed in detail by Kosterlitz and Thouless (KT) [167].

The solid on solid (SOS) model is a broken-bond many-body model that can be used to understand the roughening transition of a surface [158,160,161]. Here the surface is treated as a microscopic array of interacting atomic sites of different integer heights h_i, representing discrete atomic levels, where overhangs and voids are forbidden. There is an energy cost J when two neighboring sites differ in height by 1. Further restricting the model such that double height steps are not allowed (i.e.,

$h_i - h_j = \pm 1$) yields the restricted SOS or RSOS model. Summing over nearest neighbor pairs yields the following Hamiltonian

$$H = J \sum_{\langle i,j \rangle} |h_i - h_j|. \tag{6}$$

The roughening temperature T_r is a function of the coupling energy and shown to have a lower bound near the 2D Ising transition

$$T_r \approx \frac{J}{k_B 0.6}, \tag{7}$$

where k_B is the Boltzmann's constant [158]. The phase space mapped out by this model is composed of only two distinct surface morphologies: flat and rough. In the rough state the amplitude of the long wavelength height variations increases with temperature.

Restricting the atoms on the surface to only two height levels 0 and 1 yields another broken bond model called the lattice gas (LG) Ising model [168–171]. Here the surface is composed of a 2D matrix of sites that are either occupied or unoccupied. This model is similar to the ferromagnetic (FM) Ising model

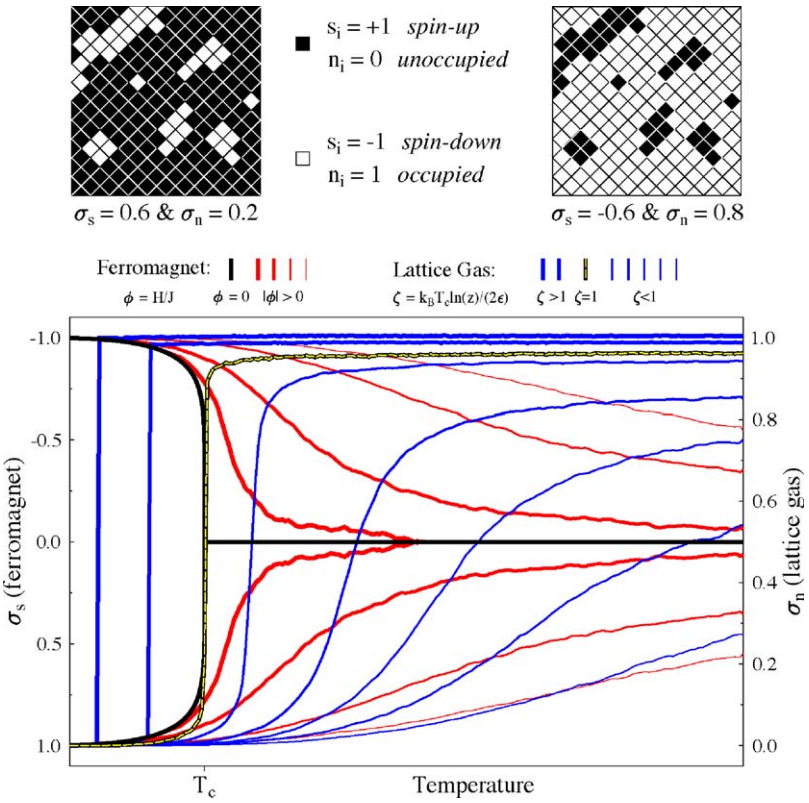

Fig. 22. Mapping of the 2D lattice-gas Ising model to the ferromagnetic model, and two possible real-space atomic configurations (above). Contrast in behaviors of the order parameters for the ferromagnetic, and lattice-gas Ising models (below). Reprinted with permission from [31], Copyright (2001) World Scientific.

with the addition that the total number of spins or atoms is allowed to fluctuate which is similar to a FM Ising model in an non-zero external field [170–172]. The differences in the thermodynamic behaviors of the order parameter for the lattice-gas and ferromagnetic Ising model are displayed in Fig. 22. The LG model has been used to successfully model order-disordered transitions for chemisorbed systems [173–177]. Here, submonolayer amounts of one species diffuse on the surface composed of different material and form a lattice gas. This model works well because the substrate provides a relatively inert template of sites for the diffusing constituents, allowing them to interact while restricting their height to one monolayer. This model has an exact (Onsager) relationship between the coupling energies and the roughening (or critical) temperature

$$\sinh\left(\frac{J_{xx}}{2k_{\mathrm{B}}T_{\mathrm{c}}}\right)\sinh\left(\frac{J_{yy}}{2k_{\mathrm{B}}T_{\mathrm{c}}}\right)=1, \tag{8}$$

where J_{xx} and J_{yy} are the asymmetric coupling energies, k_{B} the Boltzmann's constant, and T_{c} is the critical temperature [178,179]. The microscopic configuration of a many body system is characterized by a site–site correlation function for which there is also an exact solution for the Ising model [178,172]. For $T>0$ the aspect ratio of the correlation function for a symmetric Ising system ($J_{xx}=J_{yy}$) is circular and for an asymmetric system it forms an ellipse. The following equation relates the aspect ratio, AR of the correlation function to the coupling energies

$$\frac{\sinh(J_{xx}/2k_{\mathrm{B}}T_{\mathrm{c}})}{\sinh(J_{yy}/2k_{\mathrm{B}}T_{\mathrm{c}})}=(\mathrm{AR})^2. \tag{9}$$

These two equations relate the macroscopic thermodynamic behavior of the order parameter and the microscopic configuration to the coupling energies. Determining the coupling energies of an asymmetric Ising system requires the measurement of both T_{c} and AR.

The thermodynamic behavior of an Ising and RSOS system near their respective critical temperatures are different. In the language of critical phenomena they belong to different universality classes with different critical exponents, which characterize the behavior of the extensive parameters near T_{c} [180]. The critical behavior of the RSOS model is equivalent to the 2D XY spin model. In these models the phase transition is weak with a $\beta\approx\frac{1}{4}$ as compared to the Ising model with $\beta=\frac{1}{8}$, which means that the order parameter changes more abruptly for the Ising system. For example, an Ising system with a T_{c} of 800 K will experience a change of 50% in the order parameter over only 3 K, whereas an equivalent change for the RSOS system will occur over 50 K. These results demonstrate the need for accurate and reproducible temperature control when studying these phase transitions. In addition, the specific heat diverges logarithmically at T_{c} for an Ising system and only contains a finite cusp for the RSOS model [180]. These differences arise from the nature of the physical interaction that causes the phase transition. For the Ising system, the phase transition occurs due to long-range ordering of nearest neighbor pairs, whereas the XY model's phase transition occurs due to the topological interactions between vortex–antivortex pairs [167]. In the RSOS model, the topological interactions arise between steps which stiffen the surface in response to forces in the plane. This type of transition is often called a Kosterlitz–Thouless (KT) transition or a 2D liquid–solid transition.

It is *not* expected that the Ising model could be used to model the self-roughening of a surface since a real surface can readily form multi-level structures i.e., islands on top of islands [157,158]. However, in 1987 den Njis et al. presented theoretical justification that the Ising model can be used within a limited

regime to successfully model the roughening of a surface [181]. By adding an additional term to the RSOS Hamiltonian that involved energy interactions between next nearest neighbors a larger phase space is created with four distinct morphologies. One of these morphologies is called disordered flat phase which consists of an Ising-like morphology of monolayer high islands. In this model the Hamiltonian is

$$H = K_{\mathrm{NN}} \sum_{\langle r,r' \rangle} (h_r - h_{r'})^2 + L_{\mathrm{NNN}} \sum_{\langle r,r'' \rangle} (h_r - h_{r''})^2 - (\text{corner terms}), \tag{10}$$

where the heights h_r are integers, K_{NN} is the nearest neighbor coupling energy, L_{NNN} is the next nearest neighbor coupling energy, and corner terms break the symmetry between pits and islands and are left off for brevity. In a physical sense L_{NNN} can be thought of as the coupling energy between two up or two down steps on a surface. It is this extra energy cost to have two up–up or down–down steps near each other that briefly stabilizes the surface and allows it to form only one monolayer high islands. The following equation relates the next nearest neighbor coupling energy to the roughening temperature

$$\exp\left(\frac{L_{\mathrm{NNN}}}{k_{\mathrm{B}} T_{\mathrm{R}}}\right) = 2. \tag{11}$$

The phase space predicted by this Hamiltonian and three different surface morphologies are displayed in Fig. 23. In the phase plot L and K are proportional to $1/kT$ and thus at low temperatures the surface is flat. For positive nearest neighbor coupling energies one follows path 2 through a preroughening transition into a disordered flat phase with single level islands. Then the surface undergoes a KT transition to a rough surface with multi-level islands. The first transition is analogous to a gas–liquid phase transition.

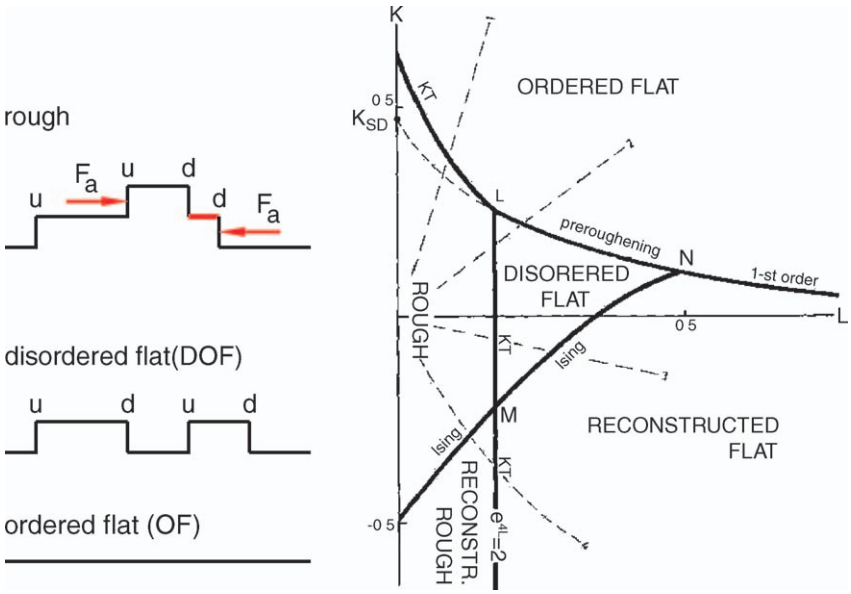

Fig. 23. (Left) Surface height cross-sections for the three phases: ordered flat (OF), disordered flat (DOF) and rough. (Right) Schematic phase diagram of the RSOS model, where L and K are proportional to $1/kT$. The dash-dotted lines represent characteristic experimental paths. Reprinted from [181], Copyright (1990) by the American Physical Society.

The second transition is analogous to a liquid solid transition where the topological interaction between similar up–up or down–down steps stiffen the surface in response to forces in the plane, eventually ''solidifying'' the surface.

4.2. Roughening of the GaAs(0 0 1)-(2 × 4) reconstructed surface

While it is hard to pin down the exact discovery of the roughening of the GaAs(0 0 1) surface, the observation and identification of the three-phase scheme of Farrell and Palmstrøm was the first systematic study to demonstrate that the structure of the surface was undergoing a change as it transitioned into the α-phase [122]. The α-phase RHEED pattern gives way to a 1 × RHEED pattern of a (2 × 1) phase at higher temperatures, for which a structural model would violate the electron counting model (cf. Fig. 2). Shortly thereafter LEED patterns could not confirm the α-phase nor the presence of the three phase scheme, suggesting that the grazing incidence of the RHEED beam or its high energy was the reason for the appearance of the α-phase RHEED pattern [54]. Four independent DFT-LDA calculations also showed that the chemical potential window for the α model was so small or even non-existent that one could effectively rule out its appearance on the surface (cf. Fig. 17) [83,85,139–141]. In addition, STM studies of surfaces prepared in the α-phase all confirmed that the atomic structure was similar to the β-phase with only two dimers in the outer most surface layer [62,65,143,13,12,144]. The only striking difference that these studies did reveal was that the α phase surfaces were more disordered than surfaces prepared in the β-phase. Recent rocking curve RHEED and RDS measurements confirmed that when in the α-phase, surfaces had the same unit cell structure when in the β-phase, namely the β2 model but with slightly different bond lengths [162,156].

Several studies measured step and kink energies using STM, which determine the roughening temperature. Pashley et al. was the first to identify, using STM, two types of steps: A and B [125]. The A steps edges run parallel to the surface As-dimers or [1 $\bar{1}$ 0] direction, with the B steps running perpendicular to A steps. After analyzing several STM images it was determined that A steps were on average straight for 10 nm with 1.6 nm kinks, while B steps were found to be very ragged with no perfectly straight regions. This indicated a large anisotropy in step energies and was later confirmed by Tanaka et al. [128].

Heller and Lagally measured a step edge anisotropy A:B of 10:1 from STM images taken after growth of GaAs on well-orientated substrates [126]. It was speculated that this resulted in a step energy ratio of 10:1. This estimate was later refined with a study that measured the decay in population of A and B steps as a function of their length [134]. To determine the step energy associated with the decay, a Boltzmann's distribution was fit to the decay from which the energies were extracted. It was found that the energies were low and ranged from $\varepsilon_A = 5$–8 meV/a_0, where a_0 is the (0 0 1) surface lattice constant of 4 Å, and $\varepsilon_B = 30$–45 meV/a_0 with a ratio of 6:1. Using a similar analysis for the kinks, their interaction was found to be repulsive with an interaction energy range 30–50 meV/a_0.

Step energies were theoretically calculated using both LCSM and DFT-LDA methods by Zhang and Zunger [140]. For A type steps for the β2 model the step formation energy was determined from LCSM to be $-0.08 - \frac{3}{8}\mu_{Ga}$ eV/(1 × 1). For B type steps for the β model the step formation energy was found to be $0.14 - \frac{1}{8}\mu_{Ga}$ eV/(1 × 1) using LCSM and $0.16 - \frac{1}{8}\mu_{Ga}$ eV/(1 × 1) using LDA. The range in μ_{Ga} for the 2 × 4 reconstruction is −0.7 to −0.2 eV. This resulted in a range of step formation energies of A: 182.5 meV/(1 × 1) to −0.005 meV/(1 × 1) and B: 227.5 meV/(1 × 1) to 165 meV/(1 × 1). While these numbers are higher than measured by Heller et al. a direct comparison with experimental results is

complicated by the broad range in chemical potentials and the two different structural models used. In addition, the ratio of energies varies from 1.2 to 33 for the range in Ga chemical potentials and is not for the same structural models. Nevertheless, these calculations give insight into the origin of the anisotropy and the computing power needed to carry out such calculations from first principles.

In a combined experimental and theoretical study of the Ga adatom concentration near typical MBE growth conditions Tersoff et al. showed that there was a surprisingly large Ga adatom concentration on the surface [182,183]. Surfaces were annealed to between 570 and 600 °C under an arsenic BEP range from 1 to 10 μTorr and then quenched to room temperature to freeze in the surface morphology. Large one monolayer high islands and monolayer deep pits were observed on the surface when imaged with in situ STM. The island coverage was measured to compute the Ga adatom concentration. By analyzing the Ga adatom concentration versus substrate temperature and arsenic BEP, it was determined that: (1) the equilibrium state of the surface was composed of monolayer high islands or pits; (2) the Ga adatom concentration decreased from 0.2 to 0.05 monolayers with decreasing substrate temperature under a constant arsenic BEP; (3) the Ga adatom concentration decreased from 0.2 to 0.05 monolayers with *increasing* arsenic BEP and constant temperature. It was shown that a one-component theoretical rate equation model could *not* reproduce both the adatom density and its temperature dependence. To correct this problem it was suggested that an effective one component model could be developed where the Ga adatom concentration would explicitly depend upon arsenic BEP. These findings indicated that during MBE growth the Ga adatom concentration maybe closer to equilibrium than previously thought.

In a series of similar but more extensive experiments, LaBella et al. measured the surface morphology using in situ STM for GaAs(0 0 1) surfaces that were annealed using band edge temperature control and then quenched to room temperature [162,31,18,163–166]. An exhaustive study of the accessible phase space was performed which included temperature ranges from 500 to 700 °C, As_4 BEPs ranging from 0.01 to 10 μTorr and annealing times from 1 min to 33 h. These studies determined that the phase transitions and surface morphologies observed were consistent with the framework of the den Njis model. More specifically, at low temperatures the surface was flat and as the temperature increased under constant As_4 BEP the surface spontaneously formed one monolayer high GaAs islands and then at higher temperatures formed multi-level islands. From measurement of the surface morphology, As_4 BEP, and substrate temperature along with application of the appropriate models, the nearest neighbor coupling energies were determined to be $\varepsilon_{[1\,\bar{1}\,0]} = 250 \pm 25$ meV and $\varepsilon_{[1\,1\,0]} = 45 \pm 5$ meV with a ratio of 5:1. In addition, the next nearest neighbor coupling energy was determined to be 50 meV.

4.2.1. Classification of surface morphologies

The degree to which the GaAs(0 0 1)-(2 × 4) roughens and the observed surface morphology is controlled by the substrate temperature and arsenic BEP. Eight filled state 1 μm × 1 μm STM images that display the change in surface morphology with annealing conditions are displayed in Fig. 24. These images are shown in gray scale where each color change represents a one monolayer height change (i.e., 0.3 nm). As the annealing points are traversed from (a) to (h) the surface transforms from a flat surface Fig. 24(a), to one with one monolayer high islands Fig. 24(b) and (c), to one with multi-level islands Fig. 24(d) and (e), back to monolayer high islands Fig. 24(f) and (g), and then back to flat Fig. 24(h). Notice how the edge of each terrace affects the formation of islands by not allowing double-height steps to form.

These surface morphologies were prepared by starting with a flat surface by annealing it at 580 °C and 10 μTorr As_4 BEP for more than 15 min then quickly switching to the annealing coordinates as indicated in the center of Fig. 24. For each annealing point, the annealing time was increased until no change in the

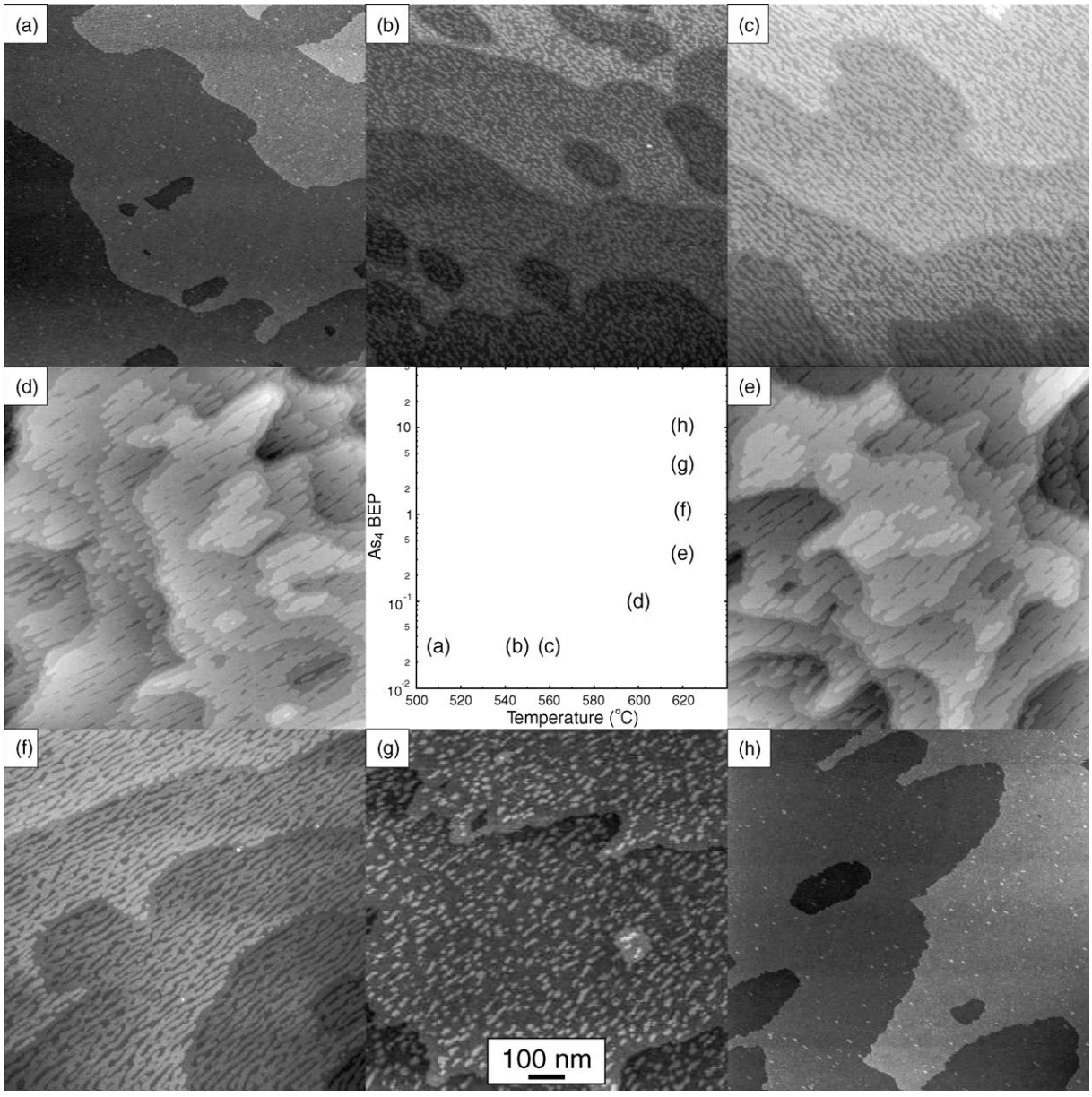

Fig. 24. Eight 1 μm × 1 μm filled state STM images of the GaAs(0 0 1)-(2 × 4) reconstructed surface prepared under different annealing conditions as indicated in the center graph. The images show the different rough morphologies: (a and h) flat; (b, c, f and g) single level islands or disordered flat; (d and e) multi-level islands or rough.

surface morphology was detected, which resulted in annealing times up to 33 h [162,166]. In addition, this time-dependent study determined that the equilibrium morphology was composed of islands and not pits. The surface was then quenched to room temperature using a procedure that freezes in the surface morphology as discussed in the Section 1. A series of images taken at a higher resolution annealed under the 1 μTorr arsenic flux showing an increase in the single level island coverage is displayed in Fig. 25.

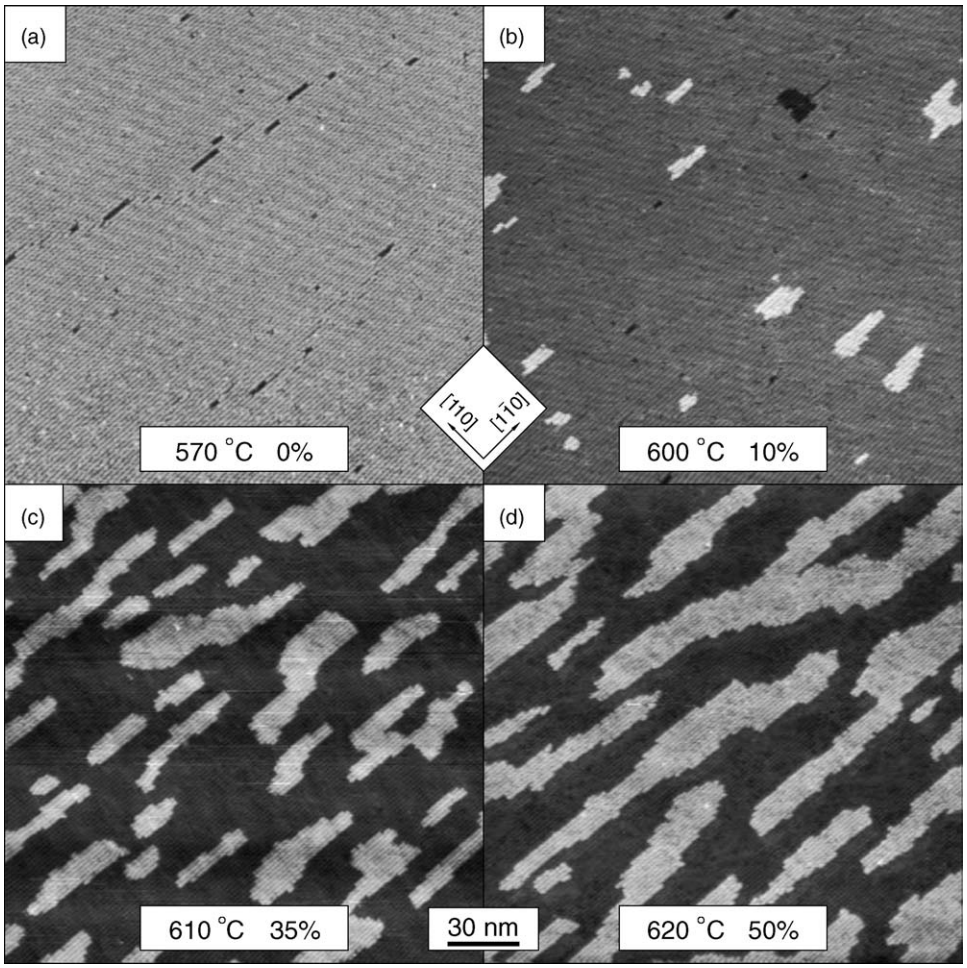

Fig. 25. Filled-state (3.0 V), 1 μm × 1 μm STM images showing the spontaneously formed islands created by annealing at the temperatures indicated and under a 0.03 μTorr As_4BEP. The coverage, ρ increases with temperature, and all the islands are elongated in direction. Reprinted with permission from [31], Copyright (2001) World Scientific.

These high-resolution images show the islands as well as the underlying rows of the (2 × 4) reconstruction. In addition, the islands are elongated in the [1 $\bar{1}$ 0] direction which is along dimer row direction of the (2 × 4) reconstruction.

Several of the surface morphologies presented in Figs. 24 and 25 are similar even though their annealing conditions are different. For example, the images in Fig. 24(a) and (h) and Fig. 25(a) have identical flat morphologies. All these surface morphologies can be classified within the den Njis framework by only considering the structure within a single terrace [cf. Fig. 23]. The morphologies in Fig. 24(a) and (h) are called ordered flat (OF) where no islands are present. The morphologies in Figs. 24(b), (c), (f) and (g) and 25(b)–(d) are called disordered flat (DOF) which consist of only up–down–up–down steps as the surface is traversed laterally, or single-level islands. The surfaces in Fig. 24(d) and (e) are called rough and consist of up–up and down–down steps or multi-level islands.

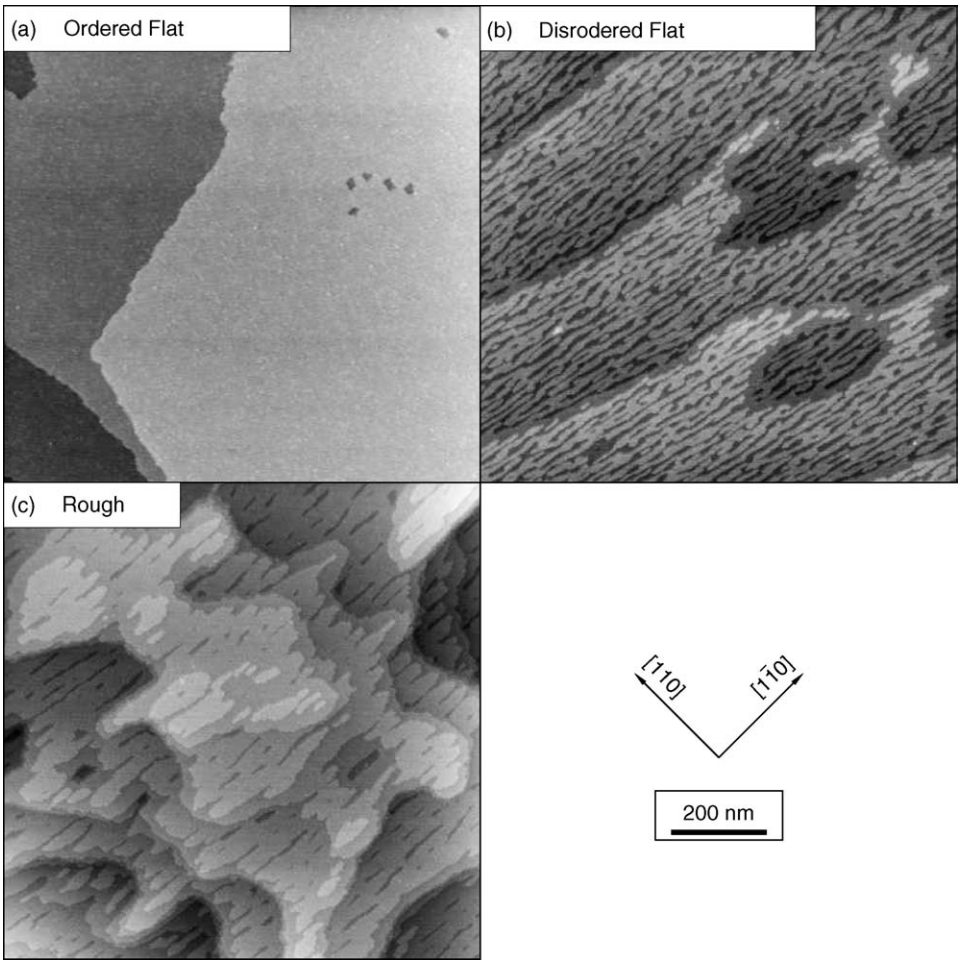

Fig. 26. (a)–(c) Three 1 μm × 1 μm filled state STM images of the GaAs(0 0 1) surface prepared under different annealing conditions. (a) 510 °C and 0.03 μTorr As_4, (b) 565 °C and 0.03 μTorr As_4showing single level islands and (c) 605 °C and 0.03 μTorr As_4 showing multilevel islands. Reprinted from [165], Copyright (2003) by the American Physical Society.

To summarize, these three distinctly different surface morphologies of the GaAs(0 0 1) surface are displayed and labeled in Fig. 26. The ordered flat surface was prepared by annealing at 510 °C and 0.03 μTorr As_4BEP and shows 1 μm wide terraces displayed in Fig. 26(a). The disordered flat surface with 2D islands was prepared by annealing the sample at 565 °C and 0.03 μTorr As_4BEP [cf. Fig. 26(b)]. All the DOF surfaces do not have double height steps and favor 2D island formation and not pit formation. This has been understood and modeled previously by assigning an energy difference to islands which have outside corners and pits which have inside corners [184,166]. The surface showing 2D islands on top of other 2D islands was prepared by annealing at 605 °C and 0.03 μTorr As_4BEP [cf. Fig. 26(c)]. Again, notice that no double-height steps exist, but more interestingly notice that the up–down–up–down step pattern is now broken. Here as one moves across the surface several up steps will occur before a down step occurs. Within the den Njis model this surface is called rough.

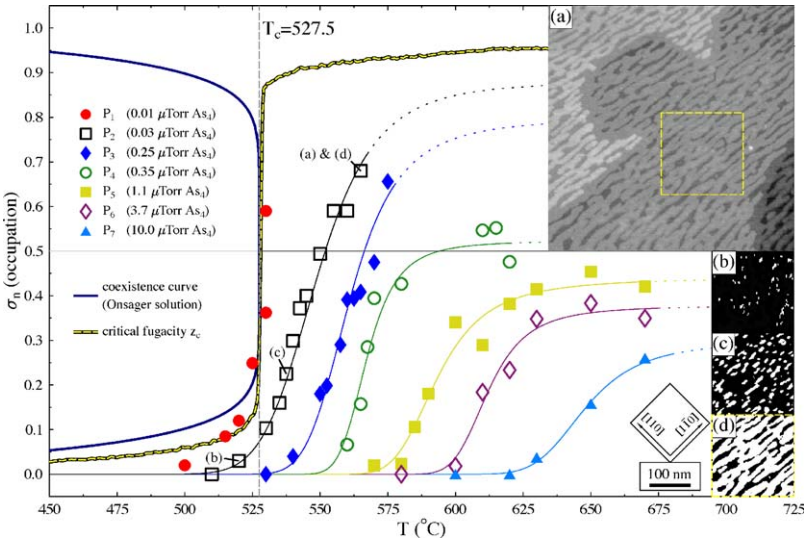

Fig. 27. The measured order parameters from the STM images as a function of temperature and applied As_4 flux as well as the coexistence curve and the curve of critical fugacity from the Monte Carlo modeling. The lines drawn through the data are best fit Fermi functions. (a) 600 nm × 600 nm STM image showing the layout of the domains on multiple terraces. (b)–(c) 200 nm × 200 nm thresholded STM images. These STM images were annealed at the temperatures indicated on the 0.03 μTorr Torr As_4 pressure series data. Reprinted with permission from [31], Copyright (2001) World Scientific.

4.2.2. Determination of coupling energies

To quantify the two phase transitions from OF to DOF (gas–liquid) and then from DOF to rough (liquid–solid) and determine the coupling energies, the phase space boundaries and island geometries must be measured. For the region where the islands remain one monolayer high a lattice gas Ising model order parameter can be used which is defined as the fractional area that the islands cover the surface. This order parameter is plotted versus temperature and As_4 flux and shown in Fig. 27. To minimize the influence of steps, ten to twenty 200 nm × 200 nm regions were cropped far from terrace edges from 5 to 10 larger images, and then thresholded to compute an average coverage, which has a uniform standard deviation of ∼5%. A series of these thresholded 200 nm × 200 nm images are shown in Fig. 27(b)–(d), which visually demonstrate the increase in coverage from 0.05 to 0.2 to 0.7, respectively, with increasing anneal temperature under a constant 0.03 μTorr As_4flux. A best fit Fermi function is drawn over each series of samples annealed under the same As_4 flux to highlight the trend. These trends agree well with the Monte Carlo simulations of the lattice gas Ising model displayed in Fig. 22 and give a T_c of 527.5 °C.

The elongation of the islands in the [1 $\bar{1}$ 0] direction indicates asymmetric coupling energies which must be quantified by computing a site–site correlation function from the STM images. A typical STM image of a GaAs(0 0 1) surface annealed at 560 °C and under a 0.03 μTorr As_4 BEP is displayed in Fig. 28(a). A smaller scale STM image of a sample annealed at 540 °C and under a 0.03 μTorr As_4 BEP is displayed in Fig. 28(b). This annealing condition shows a surface half covered with one-monolayer-high (0.28 nm) GaAs islands. The site–site correlation function computed from the STM image shown in Fig. 28(b) and displayed in Fig. 28(c). The correlation function is elongated in the same direction as the islands and a cross-section taken at 1/*e* of the maximum is an ellipse with an aspect ratio of 3 (see inset). This is a measure of the average radial island geometry. Using this value and the value of 3 for the aspect

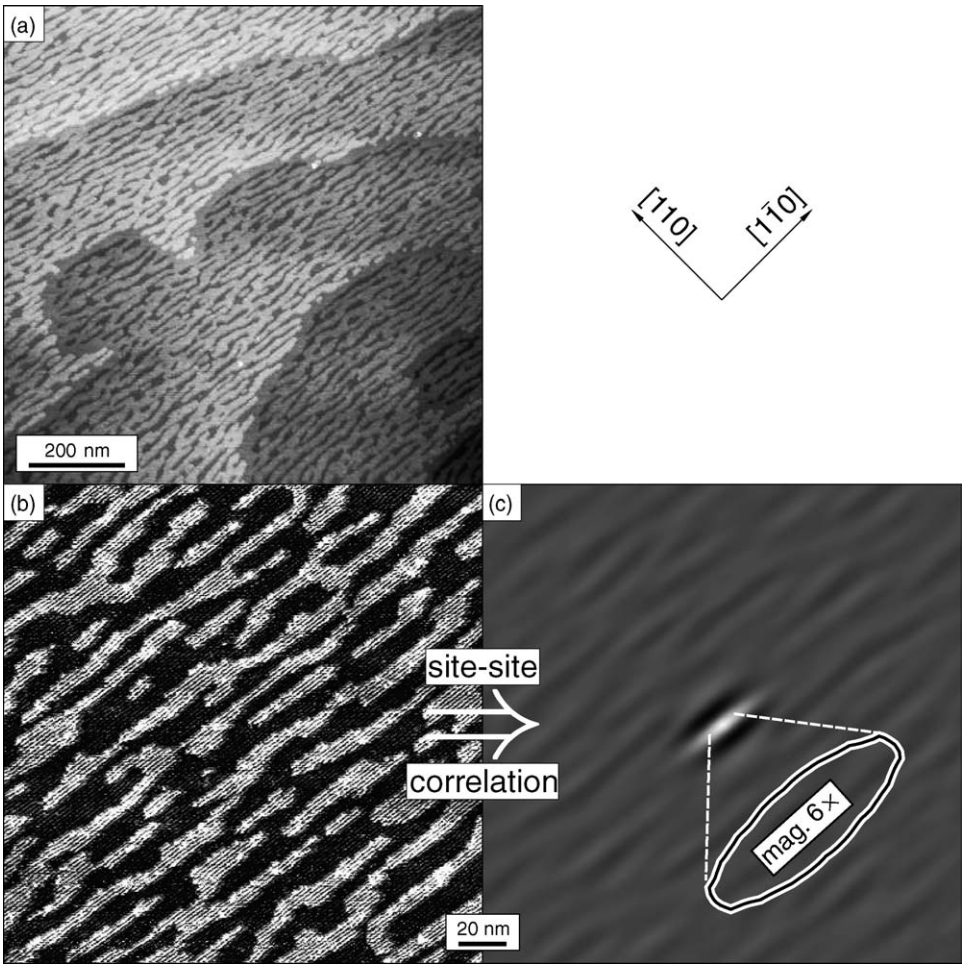

Fig. 28. (a) A 1 μm × 1 μm STM image of spontaneously formed GaAs islands annealed at 560 °C under a As_4BEP of 0.03 μTorr. (b) A 200 nm × 200 nm STM image of spontaneously formed GaAs islands annealed at 540 °C under a As_4 BEP of 0.03 μTorr. (c) A correlation function computed from image (b) shows the average geometry of the islands. (Inset) Ellipse taken at 1/*e* of the maximum showing an aspect ratio of 3. Reprinted from [162], Copyright (2000) by the American Physical Society.

ratio from Fig. 28(c), the coupling energies can be calculated from Eqs. (8) and (9) to be $\varepsilon_{[1,\bar{1}\,0]} = 250 \pm 25$ meV and $\varepsilon_{[1\,1\,0]} = 45 \pm 5$ meV with a ratio of 5:1. These values are about 5 × higher than those measured previously by Heller et al. using a different method but with good agreement in ratios and within the range of previous theoretical calculations [134,140].

The region where the surface roughens into multi-level islands cannot be plotted in Fig. 27 since the lattice gas Ising model order parameter does not apply to multi-level surfaces. The transition boundary between the DOF and rough surfaces is indicated by the solid lines turning into dashed lines. The transitions between these three distinct morphologies have been determined and plotted as function of substrate temperature and As_4 BEP and displayed in Fig. 29. At low temperatures and high As_4 BEP, the surface is free of all islands (OF) and appears similar to the image shown in Fig. 26(a). As the temperature is increased or the As_4 BEP is decreased, the surface transitions (black line with squares) to

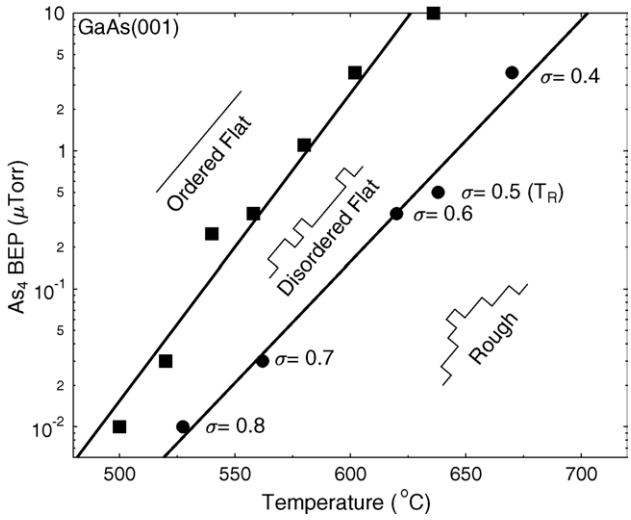

Fig. 29. Three phases of the GaAs(0 0 1) reconstructed surface prepared under different annealing conditions. The black line with squares is the boundary of ordered flat and disordered flat phases. To the left of this line, the coverage of islands is zero. The black line with circles is the transition boundary between disordered flat and rough phases. For this line the data points are also labeled with the island coverage reached just prior to roughening. Notice that this coverage varies from 80 to 40% as the substrate temperature is increased. Reprinted from [165], Copyright (2003) by the American Physical Society.

one containing only one monolayer high islands (DOF) and appears similar to the image shown in Fig. 26(b). Finally, at even higher temperatures or lower As_4 BEPs the surface transitions again (black line with circles). This time the surface contains 2D islands on top of other 2D islands (rough) and appears similar to the image shown in Fig. 26(c). Notice that even though the transition from OF to DOF is coincident with island formation, the transition from DOF to rough is more complicated. To illustrate this, the circular data points in Fig. 29 are also labeled with the coverage reached just prior to roughening. For low As_4 BEPs and low temperatures the surface needs to be 80% covered with islands before roughening. At high As_4 BEPs and high temperatures the surface needs to be only 40% covered with islands before roughening.

Even though the den Njis model does not include an external field term that is explicitly present in this data due to the arsenic flux, it still shows the full variety of surface morphologies. To determine the roughening point the As_4 BEP must be tuned to find the temperature at which the surface roughens when the coverage is 50%. The data shows this happening at 640 °C, which yields a repulsive NNN interaction energy of about 50 meV using Eq. (11). This measured value compares well with a theoretically calculated value of 50 meV for the energy of a double step on the $\beta 2(2 \times 4)$-reconstructed surface, where it was determined that the energy arose from purely electrostatics [140].

4.2.3. Role of strain on island shape

The shape of 2D islands can be affected by strain induced from the surface reconstruction and the size of the island [185]. In addition, their shape can also be influenced by the proximity of other islands. The many body Hamiltonian in Eq. (10) does not have explicit terms which account for these effects. To determine the significance of these contributions, the dependence of the aspect ratio upon coverage and the dependence of the aspect ratio upon islands size free from other islands is needed. The aspect ratio has

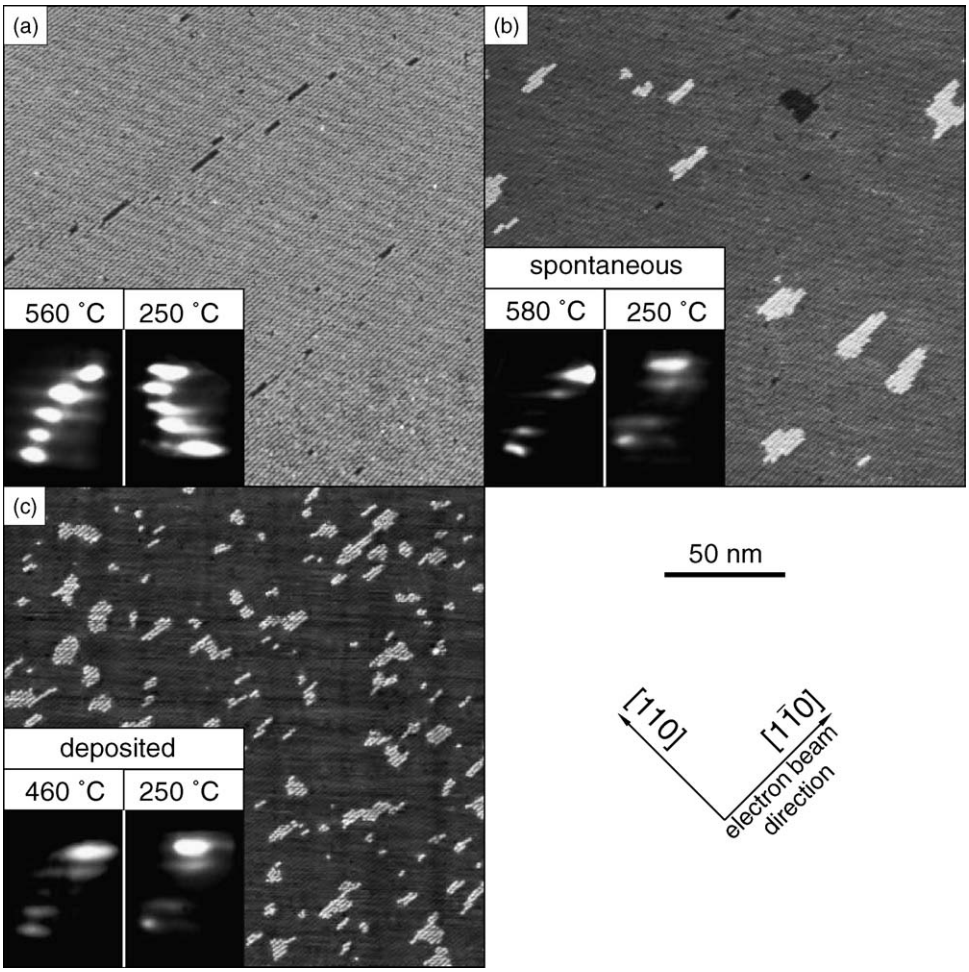

Fig. 30. (a)–(c) 200 × 200 nm filled-state STM images taken at a sample bias of −3.0 V (tunneling current: 0.1 nA) with corresponding RHEED patterns taken along the [1 $\bar{1}$ 0] direction at the indicated temperatures. (a) Flat surface showing the β-phase RHEED patterns. Surfaces covered with 10% of spontaneously formed (b) and deposited (c) one-monolayer-high islands and α-phase RHEED patterns.

been measured as a function of coverage and displayed a non-systematic variation between 2 and 3 [163]. This gives some preliminary indication that the role of strain and the presence of other islands may be small. Nevertheless, this interaction could be readily accounted for in additional terms to the Hamiltonian and may result in some adjustments to the coupling energies measured.

4.2.4. Reconciliation with RHEED patterns

Comparison of the phase diagram for the rough morphologies displayed in Fig. 29 with the RHEED phase diagram displayed in Fig. 2 shows that the onset of island formation is coincident with the onset of the α-phase RHEED pattern [18]. To clarify this, several STM images and corresponding RHEED diffraction patterns are displayed in Fig. 30. The STM image of the surface prepared in the (2 × 4)- β-phase shows a flat (2 × 4)-reconstructed surface with a low density of defects and is displayed in

Fig. 30(a). Inset in this image are two RHEED patterns taken at the temperatures indicated. These RHEED patterns are similar and show what is known as the β-phase "4-by" pattern which consists of the specular, $\frac{1}{4}, \frac{2}{4}, \frac{3}{4}$, and primary-order spots from top to bottom all with equal intensity [122]. The STM image of the surface prepared in the (2 × 4)- α-phase showing a flat surface with one-monolayer high GaAs islands that cover about 10% of the surface is displayed in Fig. 30(b). These islands have spontaneously formed on the surface due to annealing at 600 °C and 0.03 μTorr As_4 BEP as discussed previously. Inset in this image are two similar RHEED patterns showing what is known as the α-phase "4-by" pattern which is missing the $\frac{1}{2}$-order spot [122]. The STM image of the surface prepared by depositing 10% of a plane of Ga shows a flat surface having about 10% of the surface covered with one-monolayer high GaAs islands and is displayed in Fig. 30(c). The two RHEED patterns show the α-phase pattern similar to those shown in Fig. 30(b). Note, prior to deposition, the β-phase RHEED pattern was observed, identical to those shown in Fig. 30(a).

Whenever an α-phase RHEED pattern is observed at low temperatures, the STM images reveal the presence of 2D GaAs islands on the surface. This observation suggests that the α-phase diffraction pattern arises from the spontaneous formation of islands and not a change in the periodicity of the atomic structure. This is confirmed by the fact that the α model has an additional 25% of a plane of Ga compared to the β2 structural model as displayed in Fig. 15. Yet, when only 10% of a plane of Ga is deposited on a flat surface the α-phase RHEED pattern is observed. In addition, the entire 10% of a plane of Ga is accounted for by 10% of the surface being covered with GaAs islands as seen in the STM images [cf. Fig. 30(c)]. Therefore, the deposited Ga could *not* have gone into the sub-surface to form the α structural model, nor could the islands be composed of the α structural model. These findings give strong indication that the onset of the island formation is the cause of the α-phase RHEED pattern providing even more evidence that the atomic structure is still the β2 model, even though the α-phase RHEED pattern is observed.

4.2.5. Physical model

Why does a model for a single component surface work so well to explain the thermodynamics of a two component semiconducting surface with a complex multi-atom surface reconstruction such as the GaAs(0 0 1)-(2 × 4)? This behavior arises due to the interactions of Ga and As atoms with the GaAs(0 0 1) surface. Arsenic leaves the surface at lower temperatures than gallium. When the arsenic terminated GaAs(0 0 1) surface is heated the desorbing arsenic leaves behind excess Ga atoms on the surface which form a gas of atoms. It is these adatoms from the bulk which are the constituents of the lattice gas and are allowed to diffuse on the cubic (0 0 1) surface. The density of this gas can be controlled by either the substrate temperature or arsenic BEP. As the substrate temperature is increased more As atoms desorb and more Ga atoms become mobile increasing the density and chemical potential. As the As_4 BEP is increased less As atoms desorb decreasing the number of mobile Ga adatoms and thus lowering the chemical potential. Remarkably, this relative simple many body Hamiltonian provides an excellent framework for understanding this complex phenomenon of the GaAs(0 0 1) surface and possibly other (0 0 1)-oriented compound semiconductor surfaces.

5. Conclusions

The discovery of the atomic structure of the GaAs(0 0 1) surface spanned over four decades and crossed several scientific disciplines. Initiated by the desire to fabricate high-speed optoelectronic

devices understanding its surface relied on surface science, first principles ab initio calculations, and many body physics. The atomic structures of the well-ordered c(4 × 4) and (2 × 4) reconstruction are now well determined. At higher temperatures the (2 × 4) surface roughens into first a single level disordered flat phase then into a multi-level rough phase. The implications for crystal growth and epitaxy are profound in that epitaxial growth of GaAs on the GaAs(0 0 1) surface may not be an activated process ''far from equilibrium'' but one driven simply by the chemical potential gradient across the vacuum-solid interface. In addition, the highly corrugated β2 structure may aid in this process since it provides an ample number of nucleation sites in every unit cell. This knowledge may help the search for ''good'' epitaxy regimes on other surfaces and material systems.

It seems that the most interesting areas left to study on this surface is time development of the island formation process as well as the role of strain on the island shape. Recent investigations into the roughening transition using in situ RHEED and some renewed interest in theoretical modeling of the RSOS model has occurred [186,187]. Some time development studies have been carried out using in situ STM to image the formation of these islands which can occur over minutes to hours [166]. One instrument that has given profound real time insight to island formation and decay on single component surfaces is the low energy electron microscope (LEEM) [188–190]. This instrument seems well suited to investigate the island formation on GaAs(0 0 1) surface. However, the need to have an arsenic source in situ with the microscope may prove challenging.

Acknowledgements

The authors would like to thank Theodore Madey and Carl Ventrice Jr. for their support and encouragement. Special thanks to Gero Schmidt for helpful comments. This work was supported by the National Science Foundation Division of Materials Research Electronic Materials program grants: CAREER-DMR-0349108, and DMR-0405036. New York State Office of Science, Technology and Academic Research Faculty Development Program (NYSTAR-FDP-C020095), and MARCO Interconnect Focus Center.

References

[1] Z.I. Alferov, Nobel Lectures, Physics 1996–2000, World Scientific Publishing, Singapore, 2001, p. 413.
[2] J.E. Davey, T. Pankey, J. Appl. Phys. 39 (1968) 1941.
[3] J.J.R. Arthur, J. Appl. Phys. 39 (1968) 4032.
[4] J.R. Arthur, J.J. LePore, J. Vac. Sci. Technol. 6 (1969) 545.
[5] A.Y. Cho, J. Appl. Phys. 42 (1971) 2074.
[6] P. Mark, S.C. Chang, W.F. Creighton, B.W. Lee, Crit. Rev. Solid State Sci. 5 (1975) 189.
[7] W.E. Spicer, P.E. Gregory, Crit. Rev. Solid State Sci. 5 (1975) 231.
[8] M. Herman, H. Sitter, MBE, Fundamentals and Current Status, Springer, New York, 1989.
[9] M.A. Herman, H. Sitter, Molecular Beam Epitaxy, Springer, 1996.
[10] B.A. Joyce, Rep. Prog. Phys. 48 (1985) 1637.
[11] J.A. Kubby, J.J. Boland, Surf. Sci. Rep. (1996) 26.
[12] Q.-K. Xue, T. Hashizume, T. Sakurai, Appl. Surf. Sci. 141 (1999) 244.
[13] Q.-K. Xue, T. Hashizume, T. Sakurai, Prog. Surf. Sci. 56 (1997) 1.
[14] M.R. Melloch, J.M. Woodall, E.S. Harmon, N. Otsuka, D.D. Pollak, F.H. Nolte, R.M. Feenstra, M.A. Lutz, Annu. Rev. Mater. Sci. 25 (1995) 547.

[15] J.F. Whitaker, Mater. Sci. Eng. B (1993) 61.
[16] H. Ohno, A. Shen, F. Matsukura, A. Oiwa, A. Endo, S. Katsumoto, Y. Iye, Appl. Phys. Lett. 69 (1996) 363.
[17] T. Dietl, H. Ohno, Physica E 9 (2001) 185.
[18] V.P. LaBella, D.W. Bullock, C. Emery, Z. Ding, P.M. Thibado, Appl. Phys. Lett. 79 (2001) 3065.
[19] M.D. Pashley, Phys. Rev. B 40 (1989) 10481.
[20] C.B. Duke, Chem. Rev. 96 (1996) 1237.
[21] L.J. Whitman, P.M. Thibado, S.C. Erwin, B.R. Bennett, B.V. Shanabrook, Phys. Rev. Lett. 79 (1997) 693.
[22] J.E. Northrup, J. Neugebauer, R.M. Feenstra, A.R. Smith, Phys. Rev. B 61 (2000) 9932.
[23] A.R. Smith, R.M. Feenstra, D.W. Greve, M.S. Shin, M. Skowronski, J. Neugebauer, J.E. Northrup, J. Vac. Sci. Technol. B 16 (1998) 2242.
[24] R.M. Feenstra, Y. Dong, C.D. Lee, J.E. Northrup, J. Vac. Sci. Technol. B 23 (2005) 1174.
[25] E. Penev, P. Kratzer, M. Scheffler, Phys. Rev. Lett. 93 (2004) 146102.
[26] M. Krause, A. Stollenwerk, C. Awo-Affouda, B. Maclean, V.P. LaBella, J. Vac. Sci. Technol. B 23 (2005) 1684.
[27] A.N. Nesmeyanov, Vapour Pressure of Chemical Elements, Academic Press, New York, 1963.
[28] E.S. Hellman, J.S. Harris Jr., J. Cryst. Growth 81 (1987) 38.
[29] T.J. De Lyon, J.A. Roth, D.H. Chow, J. Vac. Sci. Technol. B 15 (1997) 329.
[30] J.A. Roth, J.J. Dubrary, D.H. Chow, P.D. Brewer, G.L. Olson, Indium Phosphide and Related Materials Conference Proceeding, IEEE, New Jersey, 1997, p. 253.
[31] V.P. LaBella, Z. Ding, D.W. Bullock, C. Emery, P.M. Thibado, Int. J. Mod. Phys. B 15 (2001) 2301.
[32] J.J. Harris, B.A. Joyce, P.J. Dobson, Surf. Sci. 103 (1981) L90.
[33] M. Ohring, The Material Science of Thin Films, Academic Press, New York, 1992.
[34] G. Binnig, H. Rohrer, C. Gerber, E. Weibel, Phys. Rev. Lett. 50 (1983) 120.
[35] G. Binning, H. Rohrer, C. Gerber, W. Weibel, Phys. Rev. Lett. 49 (1982) 57.
[36] L.J. Whitman, P.M. Thibado, F. Linker, J. Patrin, J. Vac. Sci. Technol. B 14 (1996) 1870.
[37] C.A. Ventrice, V.P. LaBella, L.J. Schowalter Jr., J. Vac. Sci. Technol. A 15 (1997) 830.
[38] P. Geng, J. Márquez, L. Geelhaar, J. Platen, C. Setzer, K. Jacobi, Rev. Sci. Instrum. 71 (2000) 504.
[39] J.B. Smathers, D.W. Bullock, Z. Ding, G.J. Salamo, P.M. Thibado, B. Gerace, W. Wirth, J. Vac. Sci. Technol. B 16 (1998) 3112.
[40] L.L. Chang, L. Esaki, W.E. Howard, R. Ludeke, J. Vac. Sci. Technol. 10 (1973) 11.
[41] L.L. Chang, L. Esaki, W.E. Howard, R. Ludeke, G. Schul, J. Vac. Sci. Technol. 10 (1973) 655.
[42] A.Y. Cho, J. Appl. Phys. 47 (1976) 2841.
[43] J.H. Neave, B.A. Joyce, J. Cryst. Growth 44 (1978) 387.
[44] P. Drathen, W. Ranke, K. Jacobi, Surf. Sci. 77 (1978) L162.
[45] R.Z. Bachrach, R.S. Bauer, P. Charadia, G.V. Hansson, J. Vac. Sci. Technol. 18 (1981) 797.
[46] R.Z. Bachrach, R.S. Bauer, P. Chiaradia, G.V. Hansson, J. Vac. Sci. Technol. 19 (1981) 335.
[47] P.K. Larsen, J.H. Neave, J.F. van der Veen, P.J. Dobson, B.A. Joyce, Phys. Rev. B 27 (1983) 4966.
[48] T.C. Chiang, R. Ludeke, M. Aono, G. Landgren, F.J. Himpsel, D.E. Eastman, Phys. Rev. B 27 (1983) 4770.
[49] K. Kanisawa, J. Osaka, S. Hirono, N. Inoue, J. Cryst. Growth 115 (1991) 348.
[50] C. Deparis, J. Massies, J. Cryst. Growth 108 (1991) 157.
[51] H. Norenberg, N. Koguchi, Surf. Sci. 296 (1993) 199.
[52] L. Däweritz, R. Hey, Surf. Sci. 236 (1990) 15.
[53] J. Massies, P. Etienne, F. Dezaly, N.T. Linh, Surf. Sci. 99 (1980) 121.
[54] R. Duszak, C.J. Palmstrøm, L.T. Florez, Y.N. Yang, J.H. Weaver, J. Vac. Sci. Technol. B 10 (1992) 1891.
[55] D.J. Chadi, C. Tanner, J. Ihm, Surf. Sci. 120 (1982) L425.
[56] M. Sauvage-Simkin, R. Pinchaux, J. Massies, P. Calverie, N. Jedrecy, J. Bonnet, I.K. Robinson, Phys. Rev. Lett. 62 (1989) 563.
[57] I. Kamiya, D.E. Aspnes, L.T. Florez, J.P. Harbison, Phys. Rev. B 46 (1992) 15894.
[58] C. Sasaoka, Y. Kato, A. Usui, Surf. Sci. 265 (1992) L239.
[59] C. Xu, J.S. Burnham, R.M. Braun, S.H. Goss, N. Winograd, Phys. Rev. B 52 (1995) 5172.
[60] D.K. Biegelsen, R.D. Bringans, J.E. Northrup, L.E. Swartz, Phys. Rev. B 41 (1990) 5701.
[61] I. Tanaka, S. Ohkouchi, T. Kato, F. Osaka, J. Vac. Sci. Technol. B 9 (1991) 2277.

[62] T. Hashizume, Q.K. Xue, J. Zhou, A. Ichimiya, T. Sakurai, Phys. Rev. Lett. 73 (1994) 2208.
[63] A.R. Avery, D.M. Holmes, J. Sudijono, T.S. Jones, B.A. Joyce, Surf. Sci. 323 (1995) 91.
[64] U. Resch-Esser, N. Esser, D.T. Wang, M. Kuball, J. Zegenhagen, B.O. Fimland, W. Richter, Surf. Sci. 352–354 (1996) 71.
[65] T. Hashizume, Q.K. Xue, A. Ichimiya, T. Sakurai, Phys. Rev. B 51 (1995) 4200.
[66] A.I. Shkrebtii, N. Esser, W. Richter, W.G. Schmidt, F. Bechstedt, B.O. Fimland, A. Kley, R. Del Sole, Phys. Rev. Lett. 81 (1998) 721.
[67] V.H. Etgens, M. Sauvage-Simkin, R. Pinchaux, J. Massies, N. Jedrecy, A. Waldhauer, N. Greiser, Surf. Sci. 320 (1994) 252.
[68] K. Kanisawa, H. Yamaguchi, Phys. Rev. B 56 (1997) 12080.
[69] G.R. Bell, J.G. Belk, C.F. McConville, T.S. Jones, Phys. Rev. B 59 (1999) 2947.
[70] K. Shiraishi, T. Ito, Y.Y. Suzuki, H. Kageshima, K. Kanisawa, H. Yamaguchi, Surf. Sci. 433–435 (1999) 382.
[71] J. Falta, R.M. Tromp, M. Copel, G.D. Pettit, P.D. Kirchner, Phys. Rev. Lett. 69 (1992) 3068.
[72] J. Falta, R.M. Tromp, M. Copel, G.D. Pettit, P.D. Kirchner, Phys. Rev. B 48 (1993) 5282.
[73] M.D. Pashley, J. Falta, R.M. Tromp, M. Copel, G.D. Pettit, P.D. Kirchner, Phys. Rev. Lett. 70 (1993) 3171.
[74] R. Maboudian, V. Bressler-Hill, W.H. Weinberg, J. Falta, R.M. Tromp, M. Copel, G.D. Pettit, P.D. Kirchner, Phys. Rev. Lett. 70 (1993) 3172.
[75] M. Larive, G. Jezequel, J.P. Landesman, F. Solal, J. Nagle, B. Lépine, A. Taleb-Ibrahimi, G. Indlekofer, X. Marcadet, Surf. Sci. 304 (1994) 298.
[76] G. Le Lay, D. Mao, A. Kahn, Y. Hwu, G. Margaritondo, Phys. Rev. B 43 (1991) 14301.
[77] W. Chen, M. Dumas, D. Mao, A. Kahn, J. Vac. Sci. Technol. B 10 (1992) 1886.
[78] J. Massies, P. Devoldere, N.T. Linh, J. Vac. Sci. Technol. 16 (1979) 1244.
[79] H. Hasegawa, N. Negoro, S. Kasai, Y. Ishikawa, H. Fujikuwa, J. Vac. Sci. Technol. B 18 (2000) 2100.
[80] N. Negoro, S. Kasai, H. Hasegawa, Appl. Surf. Sci. 190 (2002) 269.
[81] J.E. Northrup, S. Froyen, Phys. Rev. B 50 (1994) 2015.
[82] J.E. Northrup, S. Froyen, Phys. Rev. Lett. 71 (1993) 2276.
[83] T. Ohno, Thin Solid Films 272 (1996) 331.
[84] J.G. LePage, M. Alouani, D.L. Dorsey, J.W. Wilkins, P.E. Blöchl, Phys. Rev. B 58 (1998) 1499.
[85] N. Moll, A. Kley, E. Pehlke, M. Scheffler, Phys. Rev. B 54 (1996) 8844.
[86] A. Ohtake, J. Nakamura, S. Tsukamoto, N. Koguchi, A. Natori, Phys. Rev. Lett. 89 (2002) 206102.
[87] A. Ohtake, N. Koguchi, Appl. Phys. Lett. 83 (2003) 5193.
[88] A. Ohtake, P. Kocán, J. Nakamura, A. Natori, N. Koguchi, Phys. Rev. Lett. 92 (2004) 236105.
[89] A. Ohtake, J. Nakamura, N. Koguchi, A. Natori, Surf. Sci. 566–568 (2004) 58.
[90] M.J. Begarney, L. Li, C.H. Li, D.C. Law, Q. Fu, R.F. Hicks, Phys. Rev. B 62 (2000) 8092.
[91] N. Esser, W.G. Schmidt, C. Cobet, K. Fleischer, A.I. Shkrebtii, B.O. Fimland, W. Richter, J. Vac. Sci. Technol. B 19 (2001) 1756.
[92] A. Nagashima, M. Tazima, A. Nishimura, Y. Takagi, J. Yoshino, Surf. Sci. 493 (2001) 227.
[93] A. Nagashima, A. Nishimura, T. Kawakami, J. Yoshino, Surf. Sci. 564 (2004) 218.
[94] O. Romanyuk, P. Jiříček, M. Cukr, I. Bartoš, Surf. Sci. 566–568 (2004) 89.
[95] J.M. Ripalda, P.A. Bone, P. Howe, T.S. Jones, Surf. Sci. 540 (2003) L593.
[96] Z.M. Wang, G.J. Salamo, Phys. Rev. B 67 (2003) 125324.
[97] J. Olde, G. Mante, H. Barnscheidt, L. Kipp, J. Kuhr, R. Manzke, M. Skibowski, J. Henk, W. Schattke, Phys. Rev. B 41 (1990) 9958.
[98] T. Strasser, C. Solterbeck, W. Schattke, I. Bartoš, M. Cukr, P. Jiříček, Phys. Rev. B 63 (2001) 085309.
[99] F. Arciprete, C. Goletti, E. Placidi, P. Chiaradia, M. Fanfoni, F. Patella, C. Hogan, A. Balzarotti, Phys. Rev. B 68 (2003) 125328.
[100] C. Hogan, E. Placidi, R. Del Sole, Phys. Rev. B 71 (2005) 041308.
[101] S. Kunsági-Máté, C. Schür, T. Marek, H.P. Strunk, Phys. Rev. B 69 (2004) 193301.
[102] T. Ito, K. Tsutsumida, K. Nakamura, Y. Kangawa, K. Shiraishi, A. Taguchi, H. Kageshima, Appl. Surf. Sci. 237 (2004) 194.
[103] H. Ishizaki, T. Akiyama, K. Nakamura, K. Shiraishi, A. Taguchi, T. Ito, Appl. Surf. Sci. (2005) 186.

[104] F. Jona, IBM J. Res. Dev. 9 (1965) 375.
[105] J.R. Arthur, Surf. Sci. 43 (1974) 449.
[106] R.E. Schlier, H.E. Farnsworth, J. Chem. Phys. 30 (1959) 917.
[107] J.A. Appelbaum, G.A. Baraff, D.R. Hamann, J. Vac. Sci. Technol. 13 (1976) 751.
[108] A.J. Van Bommel, J.E. Crombeen, Surf. Sci. 57 (1976) 437.
[109] A.J. Van Bommel, J.E. Crombeen, T.G.J. Van Oirschot, Surf. Sci. 72 (1978) 95.
[110] P.K. Larsen, J.H. Neave, B.A. Joyce, J. Phys. C: Solid State Phys. (UK) 14 (1981) 167.
[111] P.K. Larsen, J.F. van der Veen, A. Mazur, J. Pollmann, J.H. Neve, B.A. Joyce, Phys. Rev. B 26 (1982) 3222.
[112] J. Ihm, D.J. Chadi, J.D. Joannopoulos, Phys. Rev. B 27 (1983) 5119.
[113] B.A. Joyce, J.H. Neave, P.J. Dobson, P.K. Larsen, Phys. Rev. B 29 (1984) 814.
[114] P.K. Larsen, P.J. Dobson, J.H. Neave, B.A. Joyce, B. Bolger, J. Zhang, Surf. Sci. 169 (1986) 176.
[115] D.J. Chadi, J. Vac. Sci. Technol. A 5 (1987) 834.
[116] D.J. Frankel, C. Yu, J.P. Harbison, H.H. Farrell, J. Vac. Sci. Technol. B 5 (1987) 1113.
[117] V.P. LaBella, H. Yang, D.W. Bullock, P.M. Thibado, P. Kratzer, M. Scheffler, Phys. Rev. Lett. 83 (1999) 2989.
[118] P.K. Larsen, D.J. Chadi, Phys. Rev. B 37 (1988) 8282.
[119] G.-X. Qian, R.M. Martin, D.J. Chadi, Phys. Rev. B 38 (1988) 7649.
[120] M.D. Pashley, K.W. Haberern, W. Friday, J.M. Woodall, P.D. Kirchner, Phys. Rev. Lett. 60 (1988) 2176.
[121] D.K. Biegelsen, R.D. Bringans, L.E. Swartz, Proc. SPIE 1186 (1990) 136.
[122] H.H. Farrell, C.J. Palmstrøm, J. Vac. Sci. Technol. B 8 (1990) 903.
[123] M.D. Pashley, K.W. Haberern, R.M. Feenstra, J. Vac. Sci. Technol. B 10 (1992) 1874.
[124] M.D. Pashley, K.W. Haberern, Ultramicroscopy 42–44 (1992) 1281.
[125] M.D. Pashley, K.W. Haberern, J.M. Gaines, Appl. Phys. Lett. 58 (1991) 406.
[126] E.J. Heller, M.G. Lagally, Appl. Phys. Lett. 60 (1992) 2675.
[127] V. Bressler-Hill, M. Wassermeier, K. Pond, R. Maboudian, G.A.D. Briggs, P.M. Petroff, W.H. Weinberg, J. Vac. Sci. Technol. B 10 (1992) 1881.
[128] I. Tanaka, S. Ohkouchi, A. Hashimoto, Jpn. J. Appl. Phys. Lett. 31 (1992) 2216.
[129] H. Tsuda, T. Mizutani, Appl. Phys. Lett. 60 (1992) 1570.
[130] M.D. Pashley, K.W. Haberern, R.M. Feenstra, P.D. Kirchner, Phys. Rev. B 48 (1993) 4612.
[131] I. Tanaka, S. Ohkouchi, Jpn. J. Appl. Phys. Lett. 32 (1993) 2152.
[132] S. Ohkouchi, N. Ikoma, I. Tanaka, J. Vac. Sci. Technol. B 12 (1994) 2030.
[133] S. Miwa, Y. Haga, E. Morita, S. Arakawa, T. Hashizume, T. Sakurai, Jpn. J. Appl. Phys. Lett. 32 (1993) 1508.
[134] E.J. Heller, Z.Y. Zhang, M.G. Lagally, Phys. Rev. Lett. 71 (1993) 743.
[135] J.M. McCoy, U. Korte, P.A. Maksym, G. Meyer-Ehmsen, Phys. Rev. B 48 (1993) 4721.
[136] T. Ohno, Phys. Rev. Lett. 70 (1993) 631.
[137] J.M. Bass, C.C. Matthai, Phys. Rev. B 50 (1994) 11212.
[138] G.P. Srivastava, S.J. Jenkins, Phys. Rev. B 53 (1996) 12589.
[139] W.G. Schmidt, F. Bechstedt, Phys. Rev. B 54 (1996) 16742.
[140] S.B. Zhang, A. Zunger, Phys. Rev. B 53 (1996) 1343.
[141] W.G. Schmidt, S. Mirbt, F. Bechstedt, Phys. Rev. B 62 (2000) 8087.
[142] S.-H. Lee, W. Moritz, M. Scheffler, Phys. Rev. Lett. 85 (2000) 3890.
[143] A. Ichimiya, Q.K. Xue, T. Hashizume, T. Sakurai, J. Cryst. Growth 150 (1995) 136.
[144] L. Broekman, R. Leckey, J. Riley, B. Usher, B. Sexton, Surf. Sci. 331–333 (1995) 1115.
[145] J. Behrend, M. Wassermeier, L. Däweritz, K.H. Ploog, Surf. Sci. 342 (1995) 63.
[146] A.R. Avery, C.M. Goringe, D.M. Holmes, J.L. Sudijono, T.S. Jones, Phys. Rev. Lett. 76 (1996) 3344.
[147] M. Takahasi, Y. Yoneda, N. Yamamoto, J. Mizuki, Phys. Rev. B 68 (2003) 085321.
[148] Y. Garreau, M. Sauvage-Simkin, N. Jedrecy, R. Pinchaux, M.B. Veron, Phys. Rev. B 54 (1996) 17638.
[149] J.M. McCoy, U. Korte, P.A. Maksym, Surf. Sci. 418 (1998) 273.
[150] Y. Liu, A.J. Komrowski, A.C. Kummel, Phys. Rev. Lett. 81 (1998) 413.
[151] P.M. Thibado, E. Kneedler, B.T. Jonker, B.R. Bennett, B.V. Shamabrook, L.J. Whitman, Phys. Rev. B 53 (1996) R10481.
[152] M. Bockstedte, A. Kley, J. Neugebauer, M. Scheffler, Comput. Phys. Commun. 107 (1997) 187.

[153] R.M. Feenstra, J.A. Stroscio, J. Tersoff, A.P. Fein, Phys. Rev. Lett. 58 (1987) 1192.
[154] R. Wiesendanger, Scanning Probe Microscopy and Spectroscopy, Methods and Applications, Cambridge University Press, Cambridge, 1994.
[155] W. Barvosa-Carter, R.S. Ross, C. Ratsch, F. Grosse, J.H.G. Owen, J.J. Zinck, Surf. Sci. 499 (2002) L129.
[156] A. Ohtake, M. Ozeki, T. Yasuda, T. Hanada, Phys. Rev. B 65 (2002) 165315.
[157] W.K. Burton, N. Cabrera, F.C. Frank, Phil. Trans. R. Soc. Lond. A: Math. Phys. Sci. (UK) (1951) 243.
[158] J.D. Weeks, in: T. Riste (Ed.), Ordering in Strongly Fluctuated Condensed Matter Systems, Plenum Press, New York, 1980, p. 293.
[159] J. Lapujoulade, Surf. Sci. Rep. 20 (1994) 191.
[160] A. Zangwill, Physics at Surfaces, Cambridge University Press, Cambridge, 1988.
[161] A. Pimpinelli, J. Villan, Physics of Crystal Growth, Cambridge University Press, Cambridge, 1998.
[162] V.P. LaBella, D.W. Bullock, M. Anser, Z. Ding, C. Emery, L. Bellaiche, P.M. Thibado, Phys. Rev. Lett. 84 (2000) 4152.
[163] V.P. LaBella, Z. Ding, D.W. Bullock, C. Emery, P.M. Thibado, J. Vac. Sci. Technol. B 19 (2001) 1640.
[164] Z. Ding, D.W. Bullock, W.F. Oliver, P.M. Thibado, V.P. LaBella, J. Cryst. Growth 251 (2003) 35.
[165] Z. Ding, D.W. Bullock, P.M. Thibado, V.P. LaBella, K. Mullen, Phys. Rev. Lett. 90 (2003) 216109.
[166] Z. Ding, D.W. Bullock, P.M. Thibado, V.P. LaBella, K. Mullen, Surf. Sci. 540 (2003) 491.
[167] J.M. Kosterlitz, D.J. Thouless, J. Phys. C: Solid State Phys. (UK) 6 (1973) 1181.
[168] F. Cerenuschi, H. Eyring, J. Chem. Phys. 7 (1939) 547.
[169] E. Ising, Z. Phys. 31 (1925) 253.
[170] T.D. Lee, C.N. Yang, Phys. Rev. 87 (1952) 404.
[171] T.D. Lee, C.N. Yang, Phys. Rev. 87 (1952) 410.
[172] B.M. McCoy, T.T. Wu, The Two-Dimensional Ising Model, Harvard University Press, Cambridge, MA, 1973.
[173] L.D. Roelofs, P.J. Estrup, Surf. Sci. 125 (1983) 51.
[174] K. Morishige, S. Kittaka, T. Morimoto, Surf. Sci. 148 (1984) 401.
[175] J. Kolackiewicz, E. Bauer, Phys. Rev. Lett. 53 (1984) 485.
[176] H.K. Kim, M.H.W. Chan, Phys. Rev. Lett. 53 (1984) 170.
[177] R.E. Ecke, J.G. Dash, Phys. Rev. B 28 (1983) 3738.
[178] L. Onsager, Phys. Rev. 65 (1944) 117.
[179] L. Onsager, Nuovo Cimento 6 (1949) 261.
[180] M.E. Fisher, Rev. Mod. Phys. 46 (1974) 597.
[181] M. den Nijs, Phys. Rev. Lett. 64 (1990) 435.
[182] M.D. Johnson, K.T. Leung, A. Birch, B.G. Orr, J. Tersoff, Surf. Sci. 350 (1996) 254.
[183] J. Tersoff, M.D. Johnson, B.G. Orr, Phys. Rev. Lett. 78 (1997) 282.
[184] M. den Nijs, K. Rommelse, Phys. Rev. B 40 (1989) 4709.
[185] V. Zielasek, F. Liu, Y. Zhao, J.B. Maxson, M.G. Lagally, Phys. Rev. B 64 (2001) 201320.
[186] Y.G. Galitsyn, D.V. Dmitriev, V.G. Mansurov, S.P. Moshchenko, A.I. Toropov, JETP Lett. 81 (2005) 766.
[187] C.C. Chien, N.-N. Pang, W.-J. Tzeng, Phys. Rev. E 70 (2004) 021602.
[188] W. Telieps, E. Bauer, Ultramicroscopy 17 (1985) 57.
[189] Y.N. Yang, E.D. Williams, R.L. Park, N.C. Bartelt, T.L. Einstein, Phys. Rev. Lett. 64 (1990) 2410.
[190] R.M. Tromp, A.W. Denier van der Gon, F.K. LeGoues, M.C. Reuter, Phys. Rev. Lett. 71 (1993) 3299.